Geophysical Journal International

Geophys. J. Int. (2017) **210,** 443–464
Advance Access publication 2017 May 1
GJI Seismology

doi: 10.1093/gji/ggx175

Instantaneous polarization analysis of ambient noise recordings in site response investigations

Vincenzo Del Gaudio

Dipartimento di Scienze della Terra e Geoambientali, Università degli Studi di Bari "Aldo Moro", Bari IT-70125, Italy. E-mail: vincenzo.delgaudio@uniba.it

Accepted 2017 April 28. Received 2017 April 26; in original form 2016 November 17

SUMMARY

A new procedure is proposed for analyses of ambient noise aimed at investigating complex cases of site response to seismic shaking. Information on site response characterized by several resonance frequencies and by amplifications varying with direction can be obtained by analysing instantaneous polarization properties of ambient noise recordings. Through this kind of analysis, it is possible to identify Rayleigh wave packets emerging from incoherent background noise for very short intervals. Analysing noise recordings passed through narrow-band filters with different central frequencies, variations of Rayleigh wave properties depending on frequencies can be estimated. In particular, one can calculate: (i) the instantaneous ratios H/V between the amplitudes of horizontal and vertical components of the elliptical particle motion and (ii) the azimuthal direction of the vertical plane containing such a motion. These can be determined on a large number of recording samples, providing the basis for statistical estimates. A preferential concentration of H/V peak values at site-specific frequencies and directions can reveal directional resonance phenomena. Furthermore, peak amplitudes can be related to site amplification factors and provide constraints for subsurface velocity modelling. Some tests, carried out on data acquired at sites with known response properties, gave indications on how to select the parameters of the analysis that optimize its implementation. In particular, preliminary trials, conducted on a limited number of frequencies, allow the selection of the parameters that, while providing a large number of instantaneous H/V estimates for Rayleigh waves, minimize their scattering. The analysis can then be refined and an H/V curve as function of frequency can be obtained with a higher spectral resolution. First tests showed that cases of directional resonance can be more effectively recognized with this technique and more details can be revealed on its properties (e.g. secondary peaks) in comparison to the Nakamura's method currently employed for ordinary noise analysis. For sites characterized by isotropic response or by differently oriented directional maxima, however, the presence of noise sources with an anisotropic spatial distribution, which excite signals with inhomogeneous distribution of energy through the examined spectral band, can make the correct interpretation of data more difficult.

Key words: Time-series analysis; Earthquake ground motions; Earthquake hazards; Seismic noise; Site effects; Surface waves and free oscillations.

1 INTRODUCTION

Damaging effects of seismic shaking can be severely increased by site response properties related to local topographic and lithological characteristics (see Kramer 1996). These can determine ground motion amplification at site-specific frequencies as an effect of resonance phenomena due to constructive interference of seismic waves at ground surface.

The most straightforward method for investigating site resonance is based on the calculation of the standard spectral ratios (SSR), that is, the average spectral ratios between ground motion recordings acquired, for the same events, at the study site and at a reference station not affected by amplification phenomena (*cf.* Borcherdt 1970). However, difficulties can be encountered in finding adequate reference sites and in acquiring, in a reasonably short lapse of time, enough data to characterize site response. These problems have stimulated the development of methods relying on the analysis of permanent signals not generated by seismic events but by other natural or anthropic sources of ground vibrations (e.g. wind impact, sea waves, car traffic and industrial machinery), commonly defined as 'ambient noise'.

The most commonly used technique exploiting ambient noise to investigate site response is the method proposed by Nakamura (1989), commonly known as HVSR (horizontal-to-vertical spectral ratio) or HVNR (horizontal-to-vertical noise ratio). It consists of the analysis of mean ratios H/V between spectral amplitudes of horizontal and vertical components of ambient noise recordings. In case of flat horizontal layering, with a high contrast of seismic impedance between a surficial soft layer and a much stiffer bedrock, site resonance properties are inferred from the observation of pronounced peaks in the curve of H/V spectral ratios.

The origin of these peaks and their relation with site response characteristics is still controversial. According to Nogoshi & Igarashi (1971), the main contribution to ambient noise derives from Rayleigh waves. Thus, H/V peaks reflect Rayleigh wave ellipticity, that is, the ratio between the horizontal and vertical components of the elliptical particle motion of these waves. In contrast, Nakamura (1989) argued that H/V peaks are directly due to *S*-wave resonance inside the surficial soft layer.

Although the opinion most commonly reported in literature attributes a major role to the ellipticity of Rayleigh waves (see discussion in Bonnefoy-Claudet *et al*. 2006a), this dispute does not condition the possibility of reliably identifying at least the resonance frequency. Indeed, for strong impedance contrast, vertical component of Rayleigh waves tends to vanish at a frequency close to that of *S*-wave resonance (Bard 1999). Therefore, whatever be the composition of ambient noise, a maximum of H/V ratios is observed around this frequency.

Another kind of site response property derivable from ambient noise analysis is the presence and the orientation of a preferential directivity. First observations of directional resonance were reported by Bonamassa & Vidale (1991) and Vidale *et al*. (1991). Subsequently, several other authors have observed similar phenomena, relating them to different morphological and geological site conditions. For instance, topographic effects were proposed to explain directional amplifications observed normally to the longer axis of hills, at wavelengths comparable with their transversal width (Spudich *et al*. 1996). In other cases, site response directivity was attributed to stiffness anisotropy, with maximum amplification transversal to fracture systems within fault zones (e.g. Martino *et al*. 2006; Pischiutta *et al*. 2012; Panzera *et al*. 2012) or to fissuring/fracturing in slopes mobilized by landslides (e.g. Del Gaudio & Wasowski 2007; Burjánek *et al*. 2010; Moore *et al*. 2011). Differently, site response directivity was observed parallel to the fault strike where wave trapping phenomena occurs within the fault zone (e.g. Cultrera *et al*. 2003).

In some of the mentioned cases, ambient noise measurements were conducted in addition to the analysis of earthquake recordings. Although the resulting H/V curves appeared often complicated by multiple peaks, an analysis of the azimuthal variation of H/V ratios revealed that major peaks are found at frequencies and directions that are consistent with frequencies and orientation of directional resonance (Burjánek *et al*. 2010; Del Gaudio *et al*., 2013, 2014).

A more complex question is the determination of the amplification factor at the resonance frequency from an H/V curve. According to the Nakamura's interpretation, body waves are directly responsible for H/V peaks, thus one could use the amplitude of these peaks to estimate amplifications. On the contrary, if H/V values are controlled by surface wave properties, they cannot be used as a measure of amplification. However, even on the latter hypothesis, information on amplification factors can be at least indirectly obtained from the ellipticity of Rayleigh waves. Indeed, the two quantities are correlated (*cf.* Konno & Ohmachi 1998; Fäh *et al*. 2001), both depending on subsurficial velocity layering. Furthermore, H/V curves, with the support of additional information (e.g. boreholes log or other geophysical data), can provide constraints to model subsoil velocities (*cf.* Castellaro & Mulargia 2009). These can then be used in numerical simulations to calculate the spectral amplification.

Some studies (e.g. Bonnefoy-Claudet *et al* 2006b; Albarello & Lunedei 2009) pointed out that ambient noise includes a mix of different types of waves (body, Rayleigh and Love waves). Their relative proportion depends on site conditions and source characteristics, which may change from case to case. Thus, the need of making assumptions about this proportion makes it more difficult to infer the characteristics of site resonance from H/V curves. In general, separating Rayleigh waves within the recorded signal can lead to obtain: (i) an estimate of the *S*-wave resonance frequencies; (ii) the recognition of site response directivity and of its orientation (from preferential directions of polarization) and (iii) some constraints for velocity modelling (from the curve of ellipticity dependence on frequency). Unfortunately, horizontal components of ambient noise can include a significant or even predominant proportion of Love waves (*cf.* Bonnefoy-Claudet *et al*. 2008), which considerably alters the H/V ratios expected for Rayleigh waves. This motivated some authors to attempt the isolation, within a noise recordings, of Rayleigh waves from Love waves, by selecting signal portions with a significant energy in the vertical component (Fäh *et al*. 2001; Poggi *et al*. 2012).

On the same line of investigations, this paper proposes an approach that, through the identification of instantaneous polarization properties, allows the identification of wave packets with Rayleigh-type particle motion within ambient noise recordings. Polarization direction and ellipticity of such waves can then be determined and the calculation of average H/V ratios at different frequencies could lead to a more reliable identification of site resonance properties. This paper first illustrates the methodological basis of the proposed technique, then reports the results of first tests carried out on noise recordings acquired at sites with known dynamic response properties. Such tests were aimed at obtaining indications for the optimization of procedural and parametric choices required by the method implementation. Test results are discussed and conclusions are drawn about potential and limits of the proposed technique.

2 METHODOLOGY

2.1 Basic principles

Rayleigh waves can be recognized within an ambient noise recording from an instant-by-instant analysis that transforms the recording into a complex-valued analytic signal. For a single-component time-series $u(t)$, its analytic representation is given by

$$u_c(t) = u(t) + j\hat{u}(t) = A(t)e^{j\Phi(t)} \quad (1)$$

where j is the imaginary unit and $\hat{u}(t)$ is the Hilbert transform of $u(t)$. According to this representation, $u(t)$ can be considered as the real part of a vector moving in a complex plane. The vector modulus $A(t)$ changes more slowly than its phase $\Phi(t)$ and can be considered as an invariant of instantaneous phase rotation. Thus, it defines an envelope modulating the quicker variations of signal due to phase changes (Morozov & Smithson 1996). Through the above-mentioned equation, one can calculate instantaneous values of $A(t)$ for different components of ground motion and compare their amplitudes.

Extending the analytic transformation to multicomponent signals, the scalar equation (1) is replaced by a vectorial equation

$$\overrightarrow{u_c}(t) = \overrightarrow{u(t)} + j\overrightarrow{\hat{u}(t)} = \overrightarrow{A(t)}\, e^{j\Phi(t)} \tag{2}$$

where $\overrightarrow{A(t)}$ is a complex vector and $\Phi(t)$ is a real phase. The multicomponent signal $\overrightarrow{u(t)}$ can be described as the projection, onto the real space, of a vector moving in a multidimensional complex space. It can be shown (Morozov & Smithson 1996) that this projection follows an elliptical trajectory, whose axes gradually change direction and length: the instantaneous elliptical trajectory lies, for bidimensional signals, on the plane of the two components, whereas, in case of 3-D signals, on a plane with variable attitude in the space.

Let be $\vec{a}(t)$ and $\vec{b}(t)$ two vectors representing the major and minor semi-axes of the instantaneous elliptical trajectories: these two vectors can be obtained by finding the phase shifts Φ_o that, applied to vector (2), maximize the modulus of its real part. Morozov & Smithson (1996) demonstrated that this is easily derived from the equation

$$\Phi_o = \frac{1}{2}\arg\left[\frac{1}{2}\sum_k (u_k + j\hat{u}_k)^2\right] \tag{3}$$

where the summation in the square brackets is extended over the two or three components u_k of the vector $\vec{u}_c(t)$ (for the cases of 2-D and 3-D signals, respectively). The ellipse semi-axes $\vec{a}(t)$ and $\vec{b}(t)$ can then be obtained from

$$\vec{a}(t) = \mathrm{Re}\left[e^{-j\Phi_o}\cdot\vec{u}_c(t)\right] \tag{4}$$

$$\vec{b}(t) = \mathrm{Re}\left[e^{-j\left(\Phi_o+\frac{\pi}{2}\right)}\cdot\vec{u}_c(t)\right]. \tag{5}$$

In the 3-D case, the attitude of the instantaneous elliptical trajectory can be defined through the so-called 'planarity vector' $\vec{p}(t)$, given by the vector product of $\vec{a}(t)$ and $\vec{b}(t)$ (Schimmel & Gallart 2003). The elliptical trajectory tends to degenerate in a rectilinear ground motion if $|\vec{a}(t)| >> |\vec{b}(t)|$. Following Schimmel & Gallart (2004), the closeness to such a condition can be measured through the rectilinearity

$$rl = 1 - \frac{\left|\vec{b}(t)\right|}{|\vec{a}(t)|}. \tag{6}$$

It assumes values between 0 and 1, which correspond to the cases of perfectly circular and linear polarizations, respectively.

2.2 Analysis procedure

The analysis of instantaneous polarization, conducted according to the principles described in the previous section, can be applied to a time-series consisting of ambient noise recording to identify Rayleigh wave packets and their characteristics (ellipticity and polarization direction). To analyse how these properties vary with frequency, one can apply the analytic transformation to time-series derived from a recording by passing it through different narrow-band filters with varying central frequency f_c. For each frequency, the analytic transformation of the two horizontal components allows obtaining, from the calculation of the vector $\vec{a}(t)$, the maximum amplitude H_{max} of ground motion on the horizontal plane and its direction. The analytic transformation of the vertical component gives a measure of its amplitude V and, dividing H_{max} by V, one obtains, at each instant and for the analysed frequency, an estimate of the ratio between the amplitude of the horizontal and vertical components of ground motion, together with the relative azimuth. The H_{max}/V ratio differs from the instantaneous ratio between horizontal and vertical components of ground motion $\overrightarrow{u(t)}$ because the latter is influenced by the different and rapidly changing phases of different components. Hereafter, the acronym HVIP will be used to indicate the method of estimating H/V ratios from instantaneous polarization analysis.

In general, a large scattering of H/V values can be expected, as the effect of the overlapping of different types of waves arriving from a spatially scattered distribution of different sources of noise. However, if one can isolate Rayleigh waves within the noise recording, these should show more coherent properties, which, as discussed in the Introduction, can be related to site response properties. To identify such signals, the analytic transformation is applied to all the three components to derive the vectors $\vec{a}(t)$ and $\vec{b}(t)$, the planarity vector $\vec{p}(t)$ and the rectilinearity *rl*. Portions of noise recording consisting of Rayleigh waves are then identified from the presence of a Rayleigh-type polarization of ground motion, that is, if (i) the instantaneous trajectories lie on a vertical plane (which implies a horizontal $\vec{p}(t)$) and (ii) one between $\vec{a}(t)$ and $\vec{b}(t)$ is horizontal, the other being vertical. If $\vec{a}(t)$ is horizontal H/V will be > 1, otherwise H/V < 1. Considering that Rayleigh waves can be contaminated by noise contributions coming from other kinds of waves, their identification does not require a perfect alignment of $\vec{p}(t)$, $\vec{a}(t)$ and $\vec{b}(t)$ with horizontal/vertical directions, but deviations can be expected. However, in order to select signal parts where Rayleigh waves are dominant (thus limiting errors in the definition of their ellipticity and polarization direction), deviations of $\vec{p}(t)$ from horizontality should not exceed an angular threshold *ldipp* and deviations of $\vec{a}(t)$ and $\vec{b}(t)$ from horizontal/vertical directions should not exceed an analogous threshold *ldipa*.

Criteria can be defined to identify Love waves as well: in this case the inclination of $\vec{a}(t)$ is required not to exceed a threshold *ldipaL*, whereas rectilinearity *rl* must be larger than a threshold *rlim* close to 1. One can note that a recording sample satisfying the identification criterion for Rayleigh waves might fit also that for Love waves if its *rl* is high. Thus, in order to define a criterion to distinguish the two kinds of waves, the threshold *rlim* is also used as a maximum limit allowed for Rayleigh wave identification. Fig. 1 shows an example of application of these criteria for the identification of Rayleigh and Love waves within a three-component recording of ambient noise.

In principle, the instantaneous polarization analysis could identify single samples of Rayleigh- or Love-type waves. However, the presence of isolated samples satisfying the identification criteria within a large amount of data might be purely casual. Thus, a more reliable identification of Rayleigh or Love waves can be obtained if a coherent type of polarization is found in more consecutive samples (e.g. at least in a number *nmin* of them). In this way, 'packets' of Rayleigh/Love waves, each consisting of not less than *nmin* samples, are identified. This procedure corresponds, in a simplified way, to the use of the degree of polarization (as defined by Schimmel & Gallart, 2003, 2004) to measure polarization stability over time and to identify Rayleigh waves in larger scale studies (e.g. Schimmel *et al*. 2011).

Finally, HVIP values obtained from Rayleigh-type wave packets (indicated as $HVIP_R$), identified within each filtered time-series, are averaged and a curve of such $\overline{HVIP_R}$ values as function of filtering central frequency f_c is assumed to represent an estimate of the Rayleigh wave ellipticity as function of frequency. The uncertainty affecting ellipticity estimates can be represented by the scatter of the instantaneous $HVIP_R$ values around their average, measured

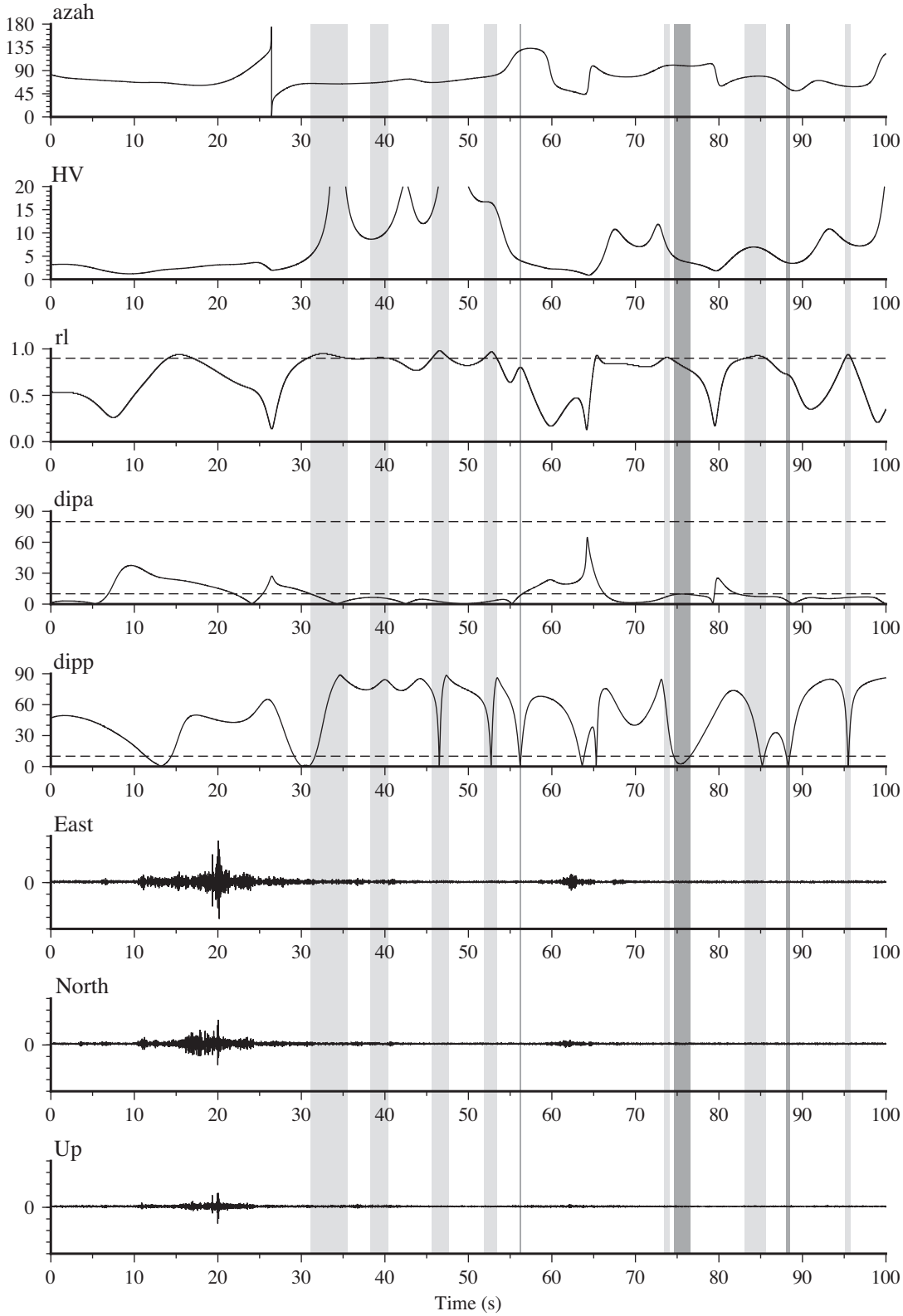

Figure 1. Example of the procedure for the identification of Rayleigh and Love wave packets within a 100 s recording of ambient noise, whose three components (east, north and up) are reported to the bottom. Diagrams show the instantaneous values of parameters obtained from the application of the HVIP technique after having passed the time-series through a Gaussian filtering centred on a frequency of 2.35 Hz. In particular: *dipp* is the inclination of $\vec{p}(t)$, *dipa* is the inclination of $\vec{a}(t)$, *rl* is the rectilinearity, HV is the H_{max}/V ratio and *azah* is the azimuth of H_{max} direction. Dashed lines mark the thresholds selected for *ldipp*, *ldipa* and *rlim*. Rayleigh waves are identified if the following conditions are simultaneously satisfied: (i) $dipp \leq ldipp = 10^{\circ}$; $dipa \leq ldipa = 10^{\circ}$ or $dipa \geq (90^{\circ} - ldipa)$ and (iii) $rl \leq rlim = 0.9$. Love waves are identified if $dipa \leq ldipaL = 10^{\circ}$ and $rl > rlim = 0.9$. Time intervals for which Rayleigh and Love waves were identified are marked in dark and light grey, respectively.

through the root mean square of $HVIP_R$ deviations from $\overline{HVIP_R}$. Examining the distribution of the azimuths of $HVIP_R$ directions, one can recognize the presence of a preferential signal polarization, which could reflect the occurrence of site response directivity.

3 IMPLEMENTATION TESTS

The implementation of the analysis method outlined in the previous section requires some decisions about the analysis procedure (e.g. type and resolution of frequency filtering) and the definition of threshold parameters for Rayleigh wave identification (*ldipp, ldipa, rlim* and *nlim*). To evaluate the method capability of recovering correct information on site response and to obtain indications about procedural and parametric choices optimizing the analysis results, ambient noise recordings acquired in the past at sites with known response properties were re-analysed using the new method.

3.1 Test sites

The test sites are located in the area of Caramanico Terme (Abruzzo region, Central Italy), where accelerometer monitoring has been conducted since 2002 to investigate the dynamic response of landslide-prone slopes to seismic shaking. These sites correspond to four stations of a local accelerometer network (Fig. 2). Two of them, named CAR2 and CAR5, were located on about 40 m thick colluvial deposits mantling a mudstone slope, which in 1989 was mobilized by a landslide (presently quiescent). CAR2 was set up on the head of this landslide, whereas CAR5 was installed on a not mobilized zone, just upslope of the landslide crown, about 150 m far from CAR2. Another station (named CAR1) was installed about 600 m NNW of CAR2, on a slope where the mudstone substratum of the landslide outcrops. Finally, a station named CAR3 was set up on 10 m thick carbonate breccias forming the rim of an about 50 m deep gorge and overlying a limestone formation.

The acquisition of several shock recordings provided data on site response properties through the comparison with the recordings of the same events, acquired at a site (named CAR4) located on a flat rocky area, about 2 km far from the others. This comparison revealed significant differences in site response, which are discussed in more detail in previous papers (Del Gaudio & Wasowski, 2007, 2011; Del Gaudio *et al*. 2008, 2013). Such differences concern the amount of the relative amplification, the resonance frequencies at which amplification is maximum and the pattern of amplification directional variations.

Estimates of spectral amplifications were derived from the calculation of SSR, using CAR4 as reference. The results obtained analysing the recordings of the events reported in Table 1 are shown in Fig. 3. In order to examine directional variation of site response, spectra of horizontal acceleration were rotated to azimuths between 5° and 355°, spaced by 10°. Spectral amplitudes were first smoothed according to Konno & Ohmachi (1998), by calculating, for each frequency f_c, a weighted average of spectral amplitudes of frequencies f differing from f_c by a factor up to $10^{\pi/40}$, with weights given by

$$W(f, f_c) = \left[\frac{\sin\left(\log_{10}\left(\frac{f}{f_c}\right)^{40}\right)}{\log_{10}\left(\frac{f}{f_c}\right)^{40}} \right]^4. \quad (7)$$

Then, the ratios between the smoothed spectra of the study sites and of the reference station in each examined direction were calculated and the results for all the events analysed were averaged.

Examining Fig. 3, differences are found in the frequencies of maximum amplification among different sites. This occurs even in the case of sites CAR2 and CAR5, despite these stations are located close each other and on the same lithology. They show similar values of the maximum amplification factors (9.4 and 8.8, respectively), but at different frequencies (2.5 and 3.3 Hz, respectively). Such resonance frequencies are likely due to the effect of the 40 m thick surficial layer of colluvium overlying the stiffer mudstone substratum. Indeed, these resonance frequencies appear quite consistent with colluvium velocities obtained by Coccia *et al*. 2010 for these sites (400 and 600 m s^{-1} for CAR2 and CAR5, respectively) through the ReMi technique (Louie 2001). Since colluvium thicknesses, estimated from borehole stratigraphies, are almost the same at the

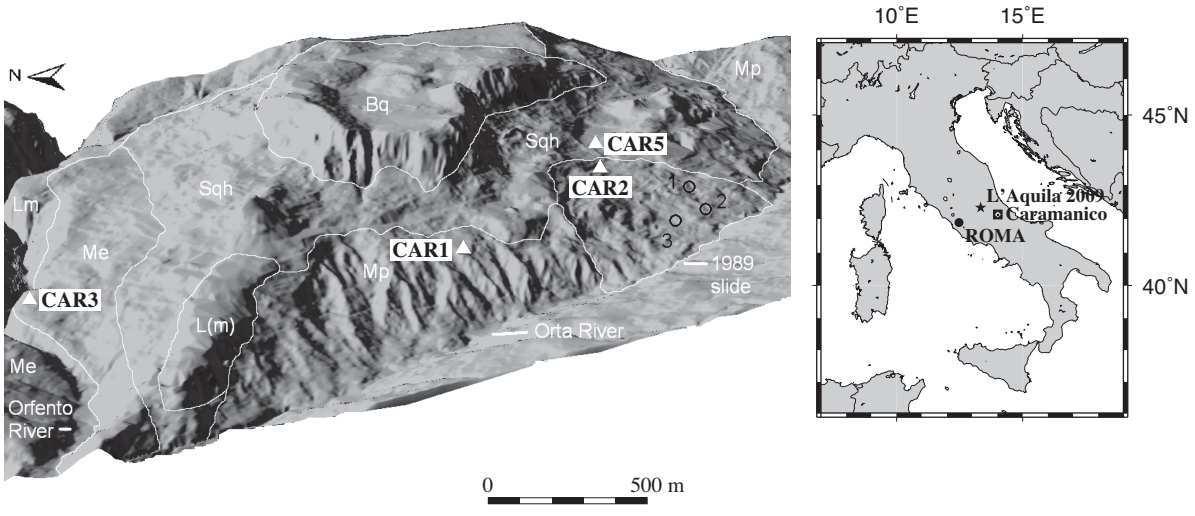

Figure 2. Digital elevation model of the Caramanico Terme test area. Geographic location is marked on inset with the epicentre of the L'Aquila 2009 earthquakes (black star). White lines mark lithological contacts and the boundary of 1989 landslide: Lm/L(m) = Limestones of Miocene/uncertain Miocene age; Me = Messinian sandy-silty deposits with carbonate breccia; Mp = Pliocene mudstones; Bq = Quaternary limestone megabreccias and Sqh = Quaternary and Holocene soils (colluvium and artificial ground). White triangles indicate the locations of the stations of the local accelerometer network, except the reference station CAR4, which is located 2.5 km SE of Caramanico (modified after Del Gaudio & Wasowski 2011).

Table 1. List of seismic events used for the calculation of the standard spectral ratios (SSR) between stations CAR1–2–3–5 and the reference station CAR4.

	Date	Time	Lat	Lon	M	Epicentral zone	Dist	Az	1	2	3	5
1	2006 March 25	05:22:44	41.726	13.897	3.1	Meta mountains	48			x		
2	2006 June 05	00:07:50	41.818	13.875	2.7	Marsica	38			x		x
3	2007 July 22	17:25:51	41.905	13.671	4.0	Marsica	39		x	x	x	x
4	2007 July 23	18:19:00	41.956	14.041	2.2	Sulmona basin	21			x		x
5	2007 October 01	17:07:10	41.996	13.984	2.1	Sulmona basin	17			x		x
6	2008 February 24	12:16:37	42.064	14.098	2.6	Maiella	12		x	x		x
7	2008 October 11	12:58:14	41.967	14.031	3.3	Sulmona Basin	20	175	x	x		
8	2009 March 29	08:42:47	41.989	14.009	3.8	Sulmona Basin	18	180	x	x	x	x
9	2009 April 06	01:32:26	42.334	13.334	6.3	L'Aquila	59	291	x	x		x
10	2009 April 06	01:36:15				not located			x	x		x
11	2009 April 06	02:37:04	42.366	13.340	4.6	L'Aquila	60	294	x	x		x
12	2009 April 06	08.53.05				not located			x	x	x	x
13	2009 April 06	13.13.54				not located			x	x	x	x
14	2009 April 06	23:15:23	42.451	13.364	4.8	Gran Sasso	63	303	x	x		x
15	2009 April 07	09:26:14	42.342	13.388	4.7	L'Aquila	55	293	x	x	x	x
16	2009 April 07	17:47:21	42.275	13.464	5.3	Aterno valley	47	288	x	x		x
17	2009 April 07	21:34:26	42.380	13.376	4.2	L'Aquila	58	297	x	x		x
18	2009 April 09	00:52:47	42.484	13.343	5.1	Gran Sasso	66	305	x	x	x	x
19	2009 April 09	03:14:44	42.338	13.437	4.2	L'Aquila	52	295	x	x	x	x
20	2009 April 09	04:32:32	42.445	13.420	4.0	Gran Sasso	59	305	x	x	x	x
21	2009 April 09	19:38:16	42.501	13.356	4.9	Gran Sasso	67	307	x	x	x	x
22	2009 April 10	14.21.32				not located				x		
23	2009 April 11	05:39:00	42.386	13.402	3.3	L'Aquila	57	298		x		x
24	2009 April 13	21:14:24	42.504	13.363	4.9	Gran Sasso	66	307	x	x	x	x
25	2009 April 21	22:26:30	41.986	14.023	3.2	Sulmona Basin	18	176		x		x
26	2009 April 23	21:49:00	42.233	13.479	4.0	Velino-Sirente	45	283	x	x	x	x
27	2009 June 22	20:58:40	42.446	13.356	4.5	Gran_Sasso	63	302	x	x	x	x
28	2009 July 31	11:05:30	42.247	13.505	3.6	Velino-Sirente	43	285		x		x
29	2009 August 06	15:36:31	41.632	13.666	3.9	Cassino zone	64	206	x	x	x	
30	2009 September 15	22:55:25	41.977	14.211	3.4	Val di Sangro	25	138	x	x	x	x
31	2009 October 08	00:51:51	41.746	13.704	3.5	Cassino zone	51	210		x		x
32	2009 October 08	00:53:38	41.738	13.706	3.4	Cassino zone	52	208	x		x	x
33	2010 January 31	08:13:55	42.245	14.065	2.7	Chieti hills	12	23		x		x
34	2011 September 10	13:15:28	41.887	13.786	2.1	Marsica	34	213				x
35	2011 December 22	22:04:33	41.999	14.012	2.5	Sulmona Basin	16	179		x		x
36	2012 July 07	10:27:41	42.066	13.966	2.6	Sulmona Basin	10	201		x		
37	2012 July 07	10:27:41	42.066	13.966	2.6	Sulmona Basin	11	196			x	x
38	2012 July 15	11:35:52	42.084	13.973	2.4	Sulmona Basin	8	202		x		x
39	2014 December 24	11:40:10	41.698	14.957	4.1	Frentani Mountains	94	123			x	

Notes: Data reported for each event are date and origin time, epicentral coordinates, magnitude, epicentral zone, epicentral distance (km) and backazimuth. In columns 1–2–3–5, a cross indicate if the event was recorded by stations CAR1–2–3–5, respectively.

two sites, the peak frequency difference seems related to changes of mechanical properties induced by the landslide on slope material. At CAR1, a maximum amplification by a factor of 6.9 is found at 6.8 Hz, whereas the largest amplification (maximum SSR = 13.6) is observed at CAR3, but at relatively high frequencies (12.6 Hz).

Another remarkable difference in site response properties concerns the directional variation of spectral amplification. Previous studies (Del Gaudio & Wasowski, 2007, 2011) reported clear evidences that CAR2 and CAR3 show a site-specific preferential orientation of maximum amplification. This can be also observed examining the percentages of the analysed frequencies having SSR maxima oriented within different azimuth intervals (Fig. 4). At CAR2, a preferential concentration is found in different frequency bands around directions with azimuth between 100° and 110° (Fig. 4a), and an even more pronounced polarization is found at CAR3 between 120° and 130° (Fig. 4b). In this latter case, a directional amplification is observed only at frequencies above 8 Hz (see Fig. 3c).

At least in the case of CAR2, the presence of a preferential direction of maximum amplification cannot be explained as the effect of source influence, since the unimodal directivity of its response does not match with the scattered distribution of the station-epicentre backazimuths (Fig. 4c). These are grouped around three different directions: one (azimuth around 120°) is mainly related to events of the 2009 L'Aquila sequence with magnitude from 3.6 to 6.3 and distances between 43 and 67 km, whereas the other two main directions (around 25° and 175°) correspond to weaker and closer events (magnitude 2.2÷3.9 and distances down to 8 km).

The directions around which SSR maxima are preferentially concentrated are also those of maximum spectral amplification. However, while at CAR3, there is a single pronounced maximum of 13.6 at 12.6 Hz (Fig. 5c), at CAR2 there are also secondary peaks larger than 7 at 1.5 and 3.4 Hz and larger than 6 at 4.8 and 6.8 Hz (Fig. 5b). Along orthogonal directions (azimuths of 15° and 35° for CAR2 and CAR3, respectively), spectral amplitudes are systematically lower and the same peaks are reduced by an amount from 20 per cent to 50 per cent (Figs 5b and c).

Comparatively, the sites CAR1 and CAR5 do not show a unique directional maximum. CAR1 (Fig. 6a) shows a multimodal distribution of azimuths of SSR peaks, associated to different frequency bands, with relative maxima at 90°–100°, mainly between 14 and

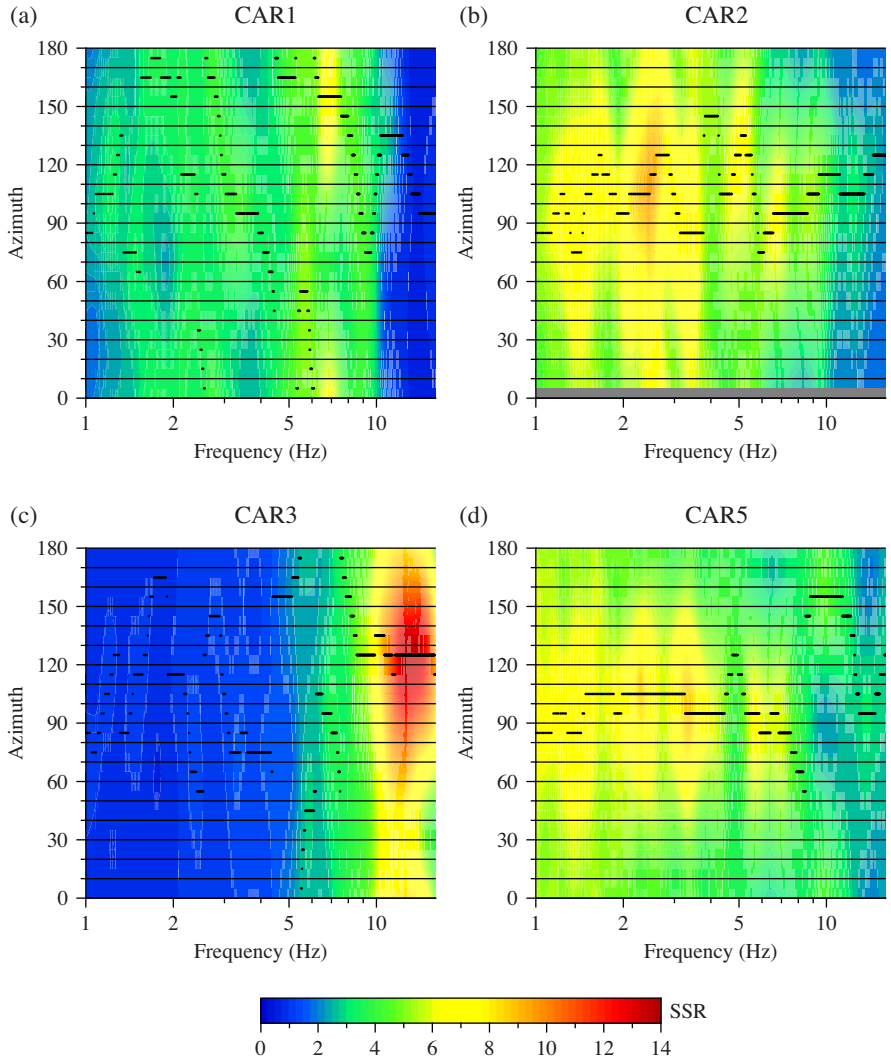

Figure 3. Standard spectral ratios (SSR) obtained by comparing seismic event recordings, acquired at each of the test sites, with the recordings of the same events at the reference site CAR4. SSR values, calculated for horizontal components with different azimuths, are reported according to the colour scale to the bottom. Black dots mark the azimuth for which maximum spectral ratio is found at each analysed frequency.

16 Hz, at 130°–140°, between 10 and 12 Hz and at 150°–160°, in the band 6–8 Hz. Only the last direction, however, corresponds to a peak of maximum amplification (6.9 at 6.8 Hz: see Figs 3a and 5a), whereas secondary SSR peaks are found along different directions (e.g. a relative maximum of 5.2 at 5.7 Hz in direction 55°). At CAR5 (Fig. 6b), the orientations of SSR maxima are mainly concentrated around two distinct directions, a principal one (95°), distributed through several frequency bands, and a secondary direction (155°), between 9 and 11 Hz. While major peaks at frequency up to 8 Hz show the first orientation, a secondary peak close to 10 Hz (Fig. 5d) is aligned according to the second azimuth.

A thorough discussion of the causes of different pattern of site response directional variations is beyond the purpose of this paper. Summarizing the results of previous studies (Del Gaudio & Wasowski, 2007, 2011; Del Gaudio *et al*., 2008, 2013), the comparison between the site response of CAR2 and CAR5 indicated that directivity at CAR2 is due to the effect of the landslide. The presence of such directivity at different frequency bands suggested that several factors acting at different scales concur to such phenomenon. For instance, the 3-D geometry of the landslide body could cause the entrapment of 2.5 Hz waves, amplified by the impedance contrast with substratum, polarizing them according to landslide lateral boundaries. At higher frequencies, ground motion amplification can be favoured by a diffuse fissuring transversal to sliding directions. At CAR3, directional amplification affects only relatively high frequencies along a direction subparallel to the gorge rim and was related to the presence of fracturing within the surficial layer of carbonate breccia, even though the reason of directivity orientation has not been clarified yet.

At CAR1 and CAR5, the presence of amplification maxima that are differently oriented at different frequencies was attributed to the occurrence of factors that amplify ground motion without a pronounced directional character. Thus, the direction of maximum ground motion is not or is only partially controlled by site properties, being influenced by wave polarization depending on source properties and propagation effect (see Del Gaudio & Wasowski 2011). In such cases, different SSR peaks show a more scattered orientation depending on the azimuthal location of the events that gave a major contribution to define the SSR at different frequencies.

Fig. 7 shows the SSR values obtained at CAR2 and CAR5 for two events (nos. 9 and 33 in Table 1), that is, the main shock of L'Aquila sequence of magnitude 6.3, occurred about 60 km WNW of

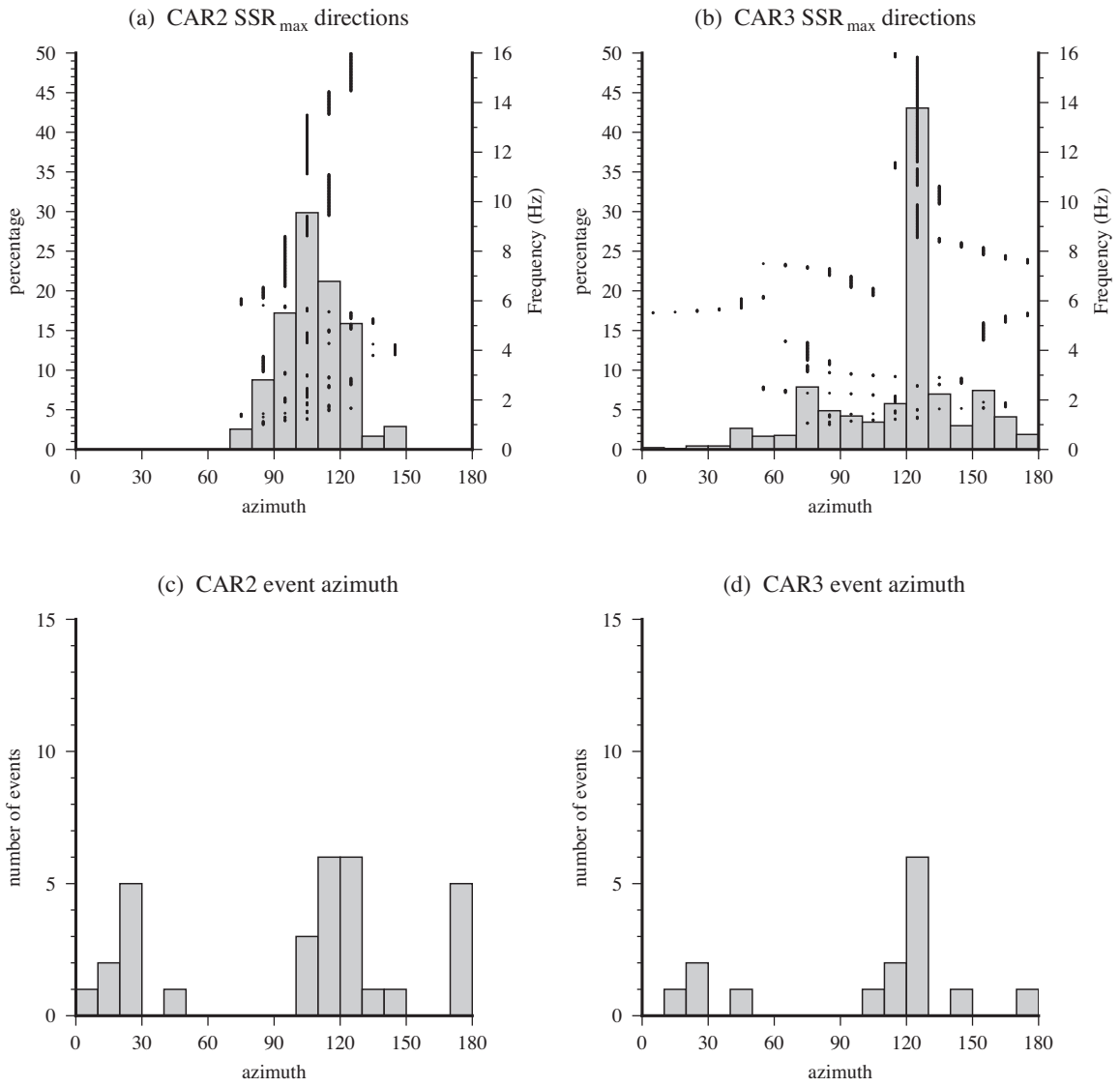

Figure 4. Top: histograms reporting the percentages of the frequencies analysed at sites CAR2 and CAR3, that have the maximum value of standard spectral ratio (SSR_{max}) oriented within different azimuth intervals of 10°. Black dots, plotted according to the frequency axis to the right, mark the frequencies having the maximum SSR oriented within the corresponding azimuth interval. As a comparison, bottom histograms show the numbers of events included in the SSR calculation, whose station-epicentre backazimuths (expressed modulo 180°) are within different azimuth intervals.

Caramanico, and a minor event of magnitude 2.7 located 12 km NNE of the study area. It is apparent that differences in magnitude and distance between these events determine the occurrence of peaks at different frequencies (higher for the smaller event). The peak orientation changes from one event to the other, being influenced by wave polarization depending on source and/or propagation effects. However, such a difference is larger for CAR5, whereas seems to be reduced at CAR2 as effect of the rotation of the 9 Hz peak towards the local direction of maximum site response. These observations suggests that a certain scattering in orientation of SSR maxima at different frequencies can be expected as effect of source-controlled polarization, but it tends to be reduced at sites where conditions of directional resonance occur.

3.2 Test results

A first test of implementation of the HVIP method on real data was conducted re-analysing ambient noise recordings acquired in 2007 during a measurement campaign carried out at Caramanico through a portable tromograph Tromino (see http://moho.world/en/ for details on this instrument). Recordings were acquired for 16 min with a rate of 128 samples per second and then analysed with the standard Nakamura's technique (Del Gaudio *et al*. 2008).

In the new analysis, data were first processed by tentatively adopting different combinations of values for the parameters of the HVIP analysis. Preliminary Gaussian filtering was carried out by multiplying the recording spectral amplitude at frequency f by a function

$$G(f) = e^{-\frac{(f-f_c)^2}{2\beta^2}}, \tag{8}$$

where f_c is the central frequency and β governs the filtering bandwidth.

At a first stage, filtering was applied around 64 central frequencies from 0.50 to 16.25 Hz, spaced by 0.25 Hz, trying six different β values (0.05, 0.1, 0.2, 0.3, 0.4 and 0.5). Furthermore, for Rayleigh wave identification, tests were carried out adopting two alternative

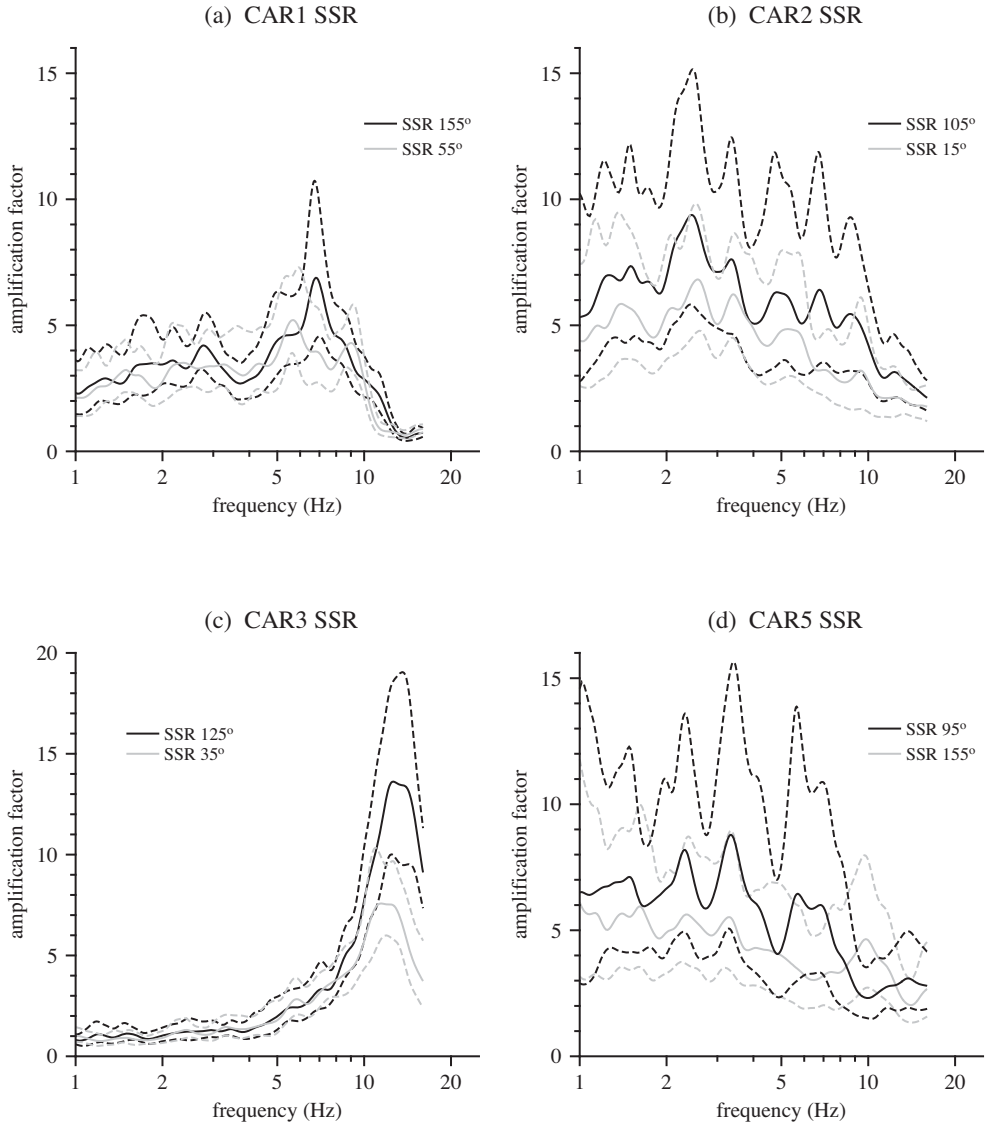

Figure 5. Curves of SSR values (solid lines) calculated for sites (a) CAR1, (b) CAR2, (c) CAR3 and (d) CAR5 as function of frequency for directions indicated in the legends. Dashed lines represent the band of spectral ratios differing from the average within a factor corresponding to the standard deviation of logarithmic residuals.

values of angular thresholds equal to 5° and 10° (identical for *ldipp* and *ldipa*), rectilinearity limits *rlim* varying from 0.90 to 0.98 and two alternative *nmin* values (15 and 20).

The first series of trials was aimed at finding the parameter combination providing a minimum scatter of $HVIP_R$ values around their averages $\overline{HVIP_R}$. However, a low scatter can result from the selection of very few wave packets. Since this weakens the reliability of the $HVIP_R$ estimates, parameter combinations resulting in the selection of less than 1 per cent of the recording data were excluded. Following this criterion, after the first series of trials, the lower value tested for the angular threshold *ldipp* (5°) was discarded and, subsequently, 10° was constantly adopted.

The definition of an *rlim* threshold for rectilinearity excludes, from $HVIP_R$ estimates, samples having Rayleigh-type polarization whose ellipticity is larger than $1/(1 - rlim)$. This implies that thresholds from 0.90 to 0.98 exclude H/V larger than a maximum permissible value varying from 10 to 50. The adoption of increasing values of *rlim* causes an increase of the $\overline{HVIP_R}$ peak value. However, such an increase becomes negligible (of the order of few tenths) beyond a certain value of *rlim*, which was finally chosen as optimal threshold. Table 2 summarizes the parameter combinations finally adopted at each site for the analysis of recordings.

In order to study in more detail the variation of Rayleigh wave ellipticity with frequency, at a second stage, noise recordings were re-analysed, using the parameters derived from the preliminary optimization tests, but reducing the step of filtering frequencies. In particular, 462 frequencies between 0.30 and 23.35 Hz, spaced by 0.05 Hz were analysed. Based on the direction of the elliptical motion, the $HVIP_R$ values were grouped into azimuth intervals of 10°. Examining the $\overline{HVIP_R}$ averages calculated for each azimuth bin as a function of filter central frequencies, considerable oscillations are found within small-frequency variations. Therefore, a Konno and Ohmachi filter was applied (Konno & Ohmachi 1998).

Finally, the smoothed mean values of Rayleigh wave ellipticity $\overline{HVIP_R}$, expressed as function of frequency and azimuth, were compared with the mean spectral ratios SSR, and also with the HVNR values derived from noise analysis carried out according to the Nakamura's method.

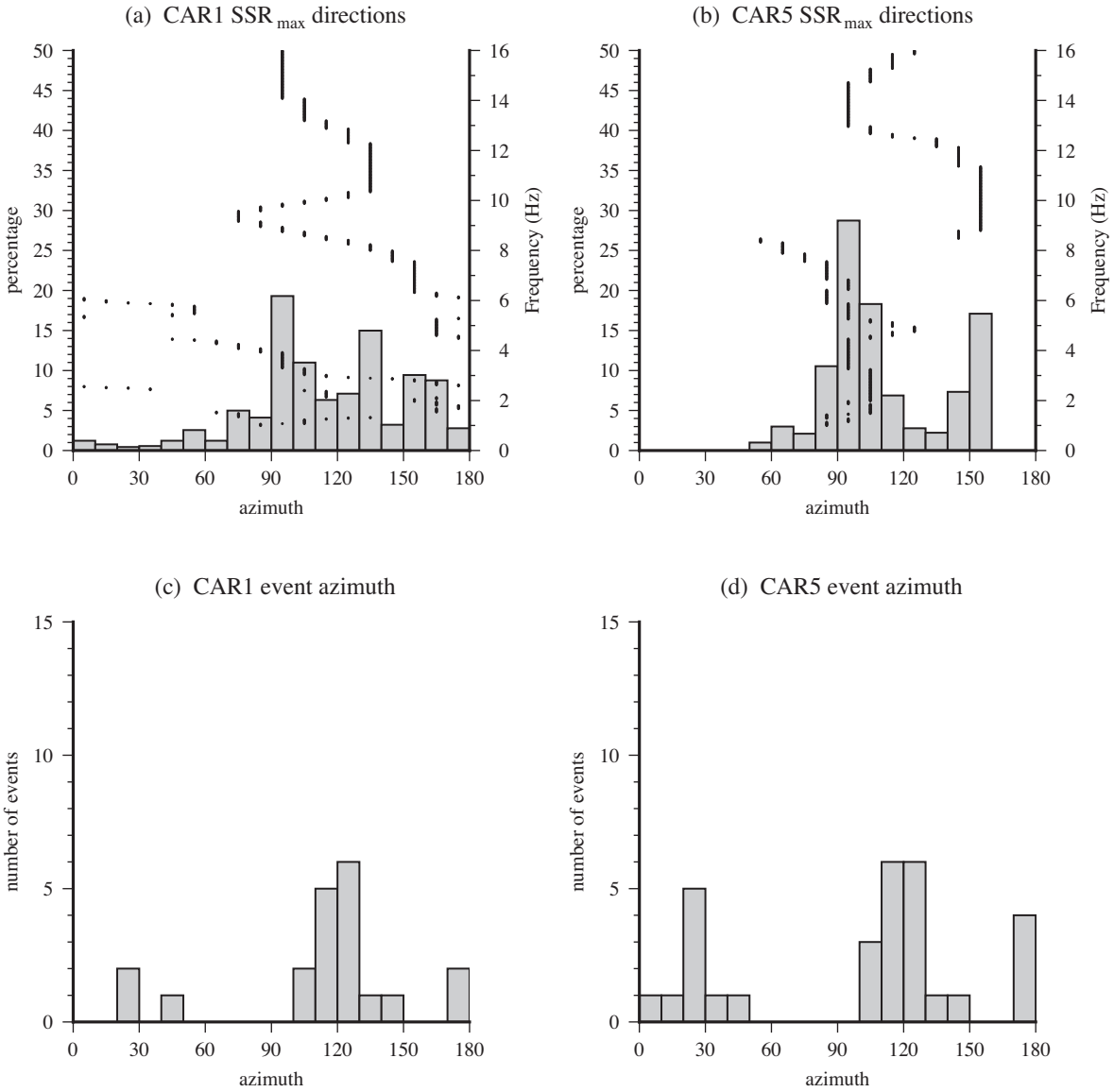

Figure 6. Top: histograms reporting the percentages of the frequencies analysed at sites CAR1 and CAR5, that have the maximum value of standard spectral ratio (SSR_{max}) oriented within different azimuth intervals of 10°. Black dots, plotted according to the frequency axis to the right, mark the frequencies having the maximum SSR oriented within the corresponding azimuth interval. As a comparison, bottom histograms show the numbers of events included in the SSR calculation, whose station-epicentre backazimuths (expressed modulo 180°) are within different azimuth intervals.

3.2.1 CAR2

The results of the HVIP analysis applied to the CAR2 recording are shown in Fig. 8. Maxima of $\overline{HVIP_R}$ at different frequencies were found to be polarized in an approximately east–west direction, according to the maxima of spectral amplification inferred from SSR (compare Figs 8b with 4a). Actually, the azimuth intervals including the largest number of maxima of $\overline{HVIP_R}$ and SSR (80°–90° and 100°–110°, respectively) differ by 20°, but this difference could reflect an influence of source-controlled wave polarization, which can deviate the direction of maximum ground motion from that of the most amplified site response. The maximum value of Rayleigh wave ellipticity was found at 2.4 Hz in the azimuth interval 90°–100°, which is in excellent agreement with the maximum of SSR found along the azimuth 105° at 2.5 Hz. More in general, comparing the curves of $\overline{HVIP_R}$ and SSR along the azimuths showing their directional maxima (Fig. 8c) a considerable similarity is found in their shape, with a good correspondence not only of the frequency of the major peak, but also of all the secondary peaks at least up to 6–7 Hz.

The presence of multiple peaks can be due both to complex site conditions and to the effect of different vibration modes. The values of $\overline{HVIP_R}$ differ significantly from those of SSR (e.g. the absolute maxima are 5.1 and 9.4, respectively), in agreement with the opinion that H/V ratios cannot be considered a direct measure of the amplification (*cf.* Bonnefoy-Claudet *et al*. 2006b; Albarello & Lunedei 2009).

At this site, it was possible to use information on subsoil characteristics, derived from previous studies, to calculate theoretical Rayleigh wave ellipticity through a 1-D modelling and thus to verify the plausibility of the HVIP analysis results. For this purpose, the code *gpell* (Wathelet 2005) was used, which was developed in the framework of the European project SESAME (Site EffectS assessment using Ambient Excitations: see www.geopsy.org). Modelling

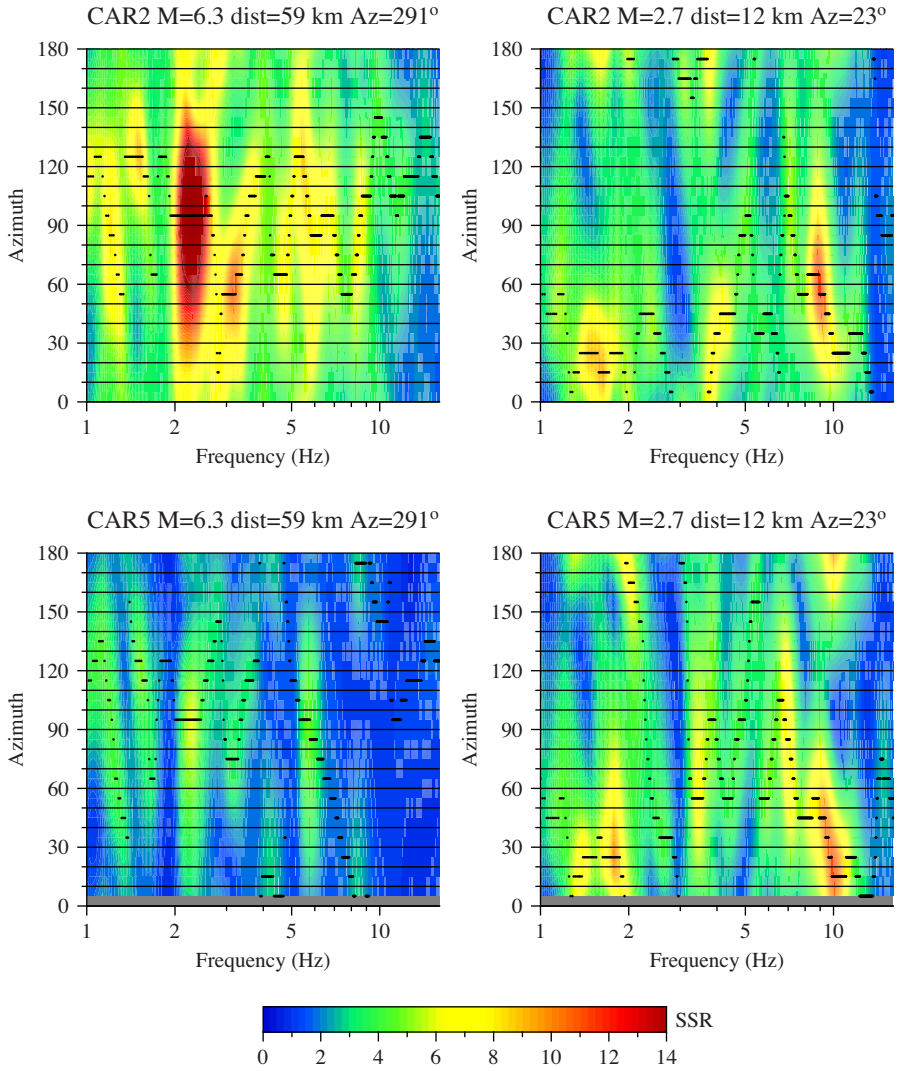

Figure 7. Standard spectral ratios (SSR) calculated at sites CAR2 and CAR5 for the main shock of the 2009 L'Aquila sequence of magnitude 6.3. (to the left) and for a minor event of magnitude 2.7 occurred 12 km from the sites (Az is the backazimuth station epicentre). Black dots mark the azimuth for which maximum spectral ratio was found at each analysed frequency.

Table 2. HVIP analysis parameters selected through the preliminary tests: β = parameter controlling the filtering bandwidth; *ldipp* = maximum permissible inclination for planarity vector; *nmin* = minimum number of consecutive samples with coherent polarization used to identify Rayleigh wave packets and *rlim* = rectilinearity thresholds used to distinguish Rayleigh from Love waves.

Site	β	*ldipp*	*nmin*	*rlim*	nR_{av}	%	*nRp*	Scatter
CAR1	0.50	10°	20	0.90	1354	1.1	33 ± 3	1.5
CAR2	0.05	10°	20	0.90	3369	2.8	115 ± 23	1.4
CAR3	0.10	10°	20	0.97	2555	2.1	57 ± 12	2.6
CAR5	0.30	10°	20	0.90	1512	1.2	39 ± 4	1.5

Notes: Some characteristics of the resulting set of Rayleigh-type data are also shown: nR_{av} = average number of Rayleigh-type data over all the frequencies analysed; % = percentage of recording data classified as Rayleigh-type; *nRp* = number of data forming Rayleigh wave packets (average ± standard deviation); scatter = root mean square of deviations of $HVIP_R$ values from the average $\overline{HVIP_R}$ calculated for each frequency.

was based on data derived from boreholes and seismic refraction profiles (Buccolini *et al*. 1995) and from ReMi surveys (Coccia *et al*. 2010). In particular, borehole stratigraphy allowed to constrain subsoil layer thicknesses, laboratory measurements on few samples provided density data, *P*-wave velocities were derived from seismic refraction and *S*-wave velocities from ReMi surveys. Starting from these data, ellipticity curves for the fundamental and first higher mode of Rayleigh waves were modelled. They appear quite consistent with the ellipticity peaks at 2.4 and 3.6 Hz in the $\overline{HVIP_R}$ curve (corresponding to the two largest peaks of SSR), as shown in Fig. 9.

The H/V curve obtained with the HVIP analysis was also compared with the one obtained analysing the same noise recording with the Nakamura's (1989) method. At this regard, data were processed following the recommendations proposed by the project SESAME (Bard & the SESAME Team 2004) for a standardization of the calculation procedure. In particular: (1) noise recording was

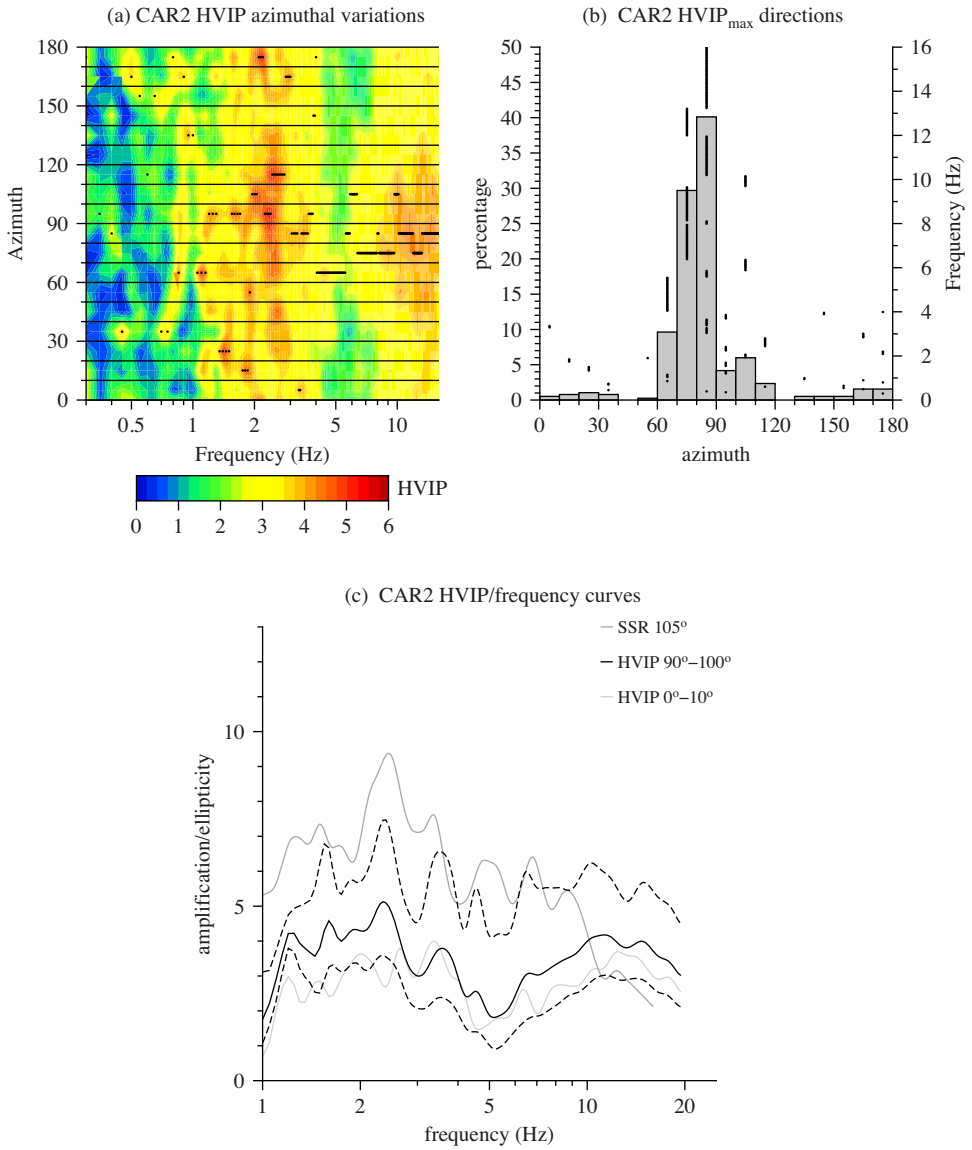

Figure 8. Results of the HVIP analysis of the noise recording acquired at CAR2. Diagram (a) reports mean values of Rayleigh wave ellipticity ($\overline{HVIP_R}$) as function of frequency and azimuth. Histogram (b) shows the percentages of the frequencies having $\overline{HVIP_R}$ maximum directed within different azimuth intervals. Both in (a) and (b), black dots mark the azimuth for which the maximum spectral ratio was found at each analysed frequency. Diagram (c) reports the curves of $\overline{HVIP_R}$ as function of frequency for the azimuths 90°–100° (black solid line) and 0°–10° (light grey thick line). For the former, the black dashed lines delimit the band of variability of $HVIP_R$ values within one standard deviation (in logarithmic residuals) from the average $\overline{HVIP_R}$. For comparison purposes, the SSR curve corresponding to maximum amplification is also shown (dark grey thin line).

partitioned into 30 s time windows, excluding those showing anomalous H/V ratios (differing from the average by more than three times the standard deviation); (2) spectra of horizontal and vertical components were smoothed using a Konno and Ohmachi filter; (3) the geometric mean of the two horizontal components was calculated and divided by the spectral amplitude of the vertical component for each time window and (4) the spectral ratios HVNR derived from all time windows were averaged. Additionally, directional variations of spectral ratios were examined by calculating the HVNR values for horizontal components with azimuths between 5° and 355° spaced by 10°.

Fig. 10 shows the obtained results. The histogram in Fig. 10(b) shows the distribution of azimuths of HVNR maxima found in the directional analysis at different frequencies. One can note that, consistently with the results of the HVIP analysis, there is a strong concentration of these maxima oriented with azimuth of 85°, which is also the direction of maximum HVNR, found at a frequency of 2.4 Hz. This confirms that the analysis of the HVNR directional variations can point out frequency and orientation of directional resonance. However, the HVNR curves (Fig. 10c) show considerably lower values of H/V ratios in comparison to HVIP. Furthermore, even though the main peak at 2.4 Hz can be recognized, less details are provided about the other secondary peaks (e.g. the peak relative to the first higher mode at 3.6 Hz), which may not be clearly distinguished. The underestimate of the H/V ratios appears particularly pronounced if HVNR values are calculated as geometric mean of the horizontal components: with such a procedure H/V maximum would be estimated equal to about 3, thus suggesting the occurrence of moderate amplification conditions. This indicates that the use of the geometric mean to derive a single H/V curve, in case of sites

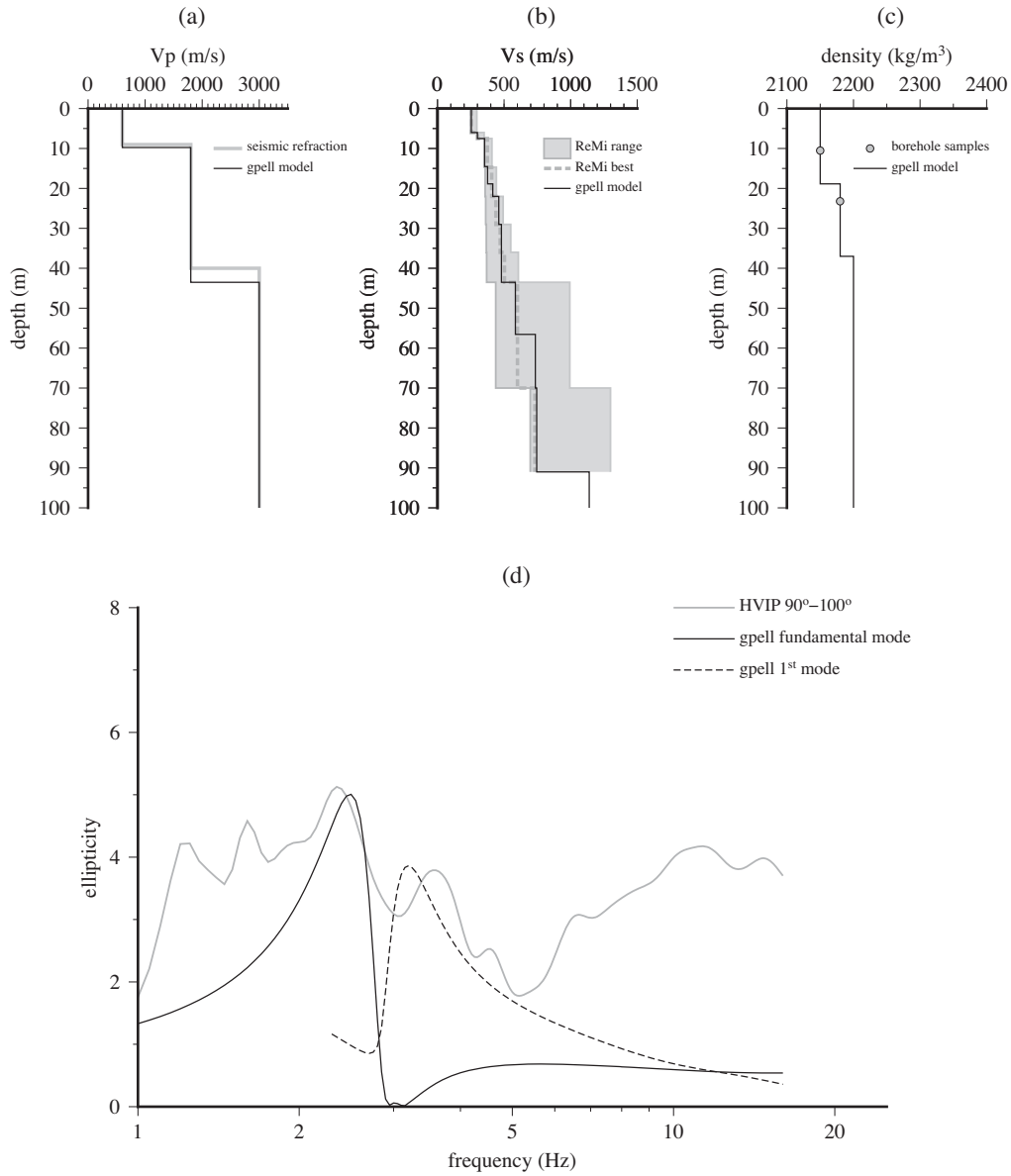

Figure 9. Data and results of the modelling of Rayleigh wave ellipticity. Diagram (a) shows *P*-wave velocities derived from seismic refraction profiles, reported in Buccolini *et al*. (1995) (grey line) and the profile assumed in this model (black line). Diagram (b) reports the *S*-wave velocities derived from ReMi surveys by Coccia *et al*. (2010) (dashed line = best-fit model and grey area = range of velocity solutions compatible with data) and the velocity vertical profile assumed in this model (black line). Diagram (c) compares densities obtained by Buccolini *et al*. (1995) from measurements on samples derived from borehole (grey dots) and the vertical distribution of density values assumed in this model (black line). In diagram (d), ellipticities estimated from the HVIP analysis (grey line) are compared with the curves calculated through the code *gpell* (black solid line = fundamental mode and dashed line = first higher mode).

affected by a pronounced directivity in dynamic response, can be rather misleading.

3.2.2 CAR5

Applying the HVIP analysis to the CAR5 recording, some problems arise from the difficulty of selecting a single $\overline{\text{HVIP}_\text{R}}$ curve that can be considered completely representative of the site response properties. Indeed, examining the directional distribution of $\overline{\text{HVIP}_\text{R}}$ maxima, there is not a single strong preferential direction (Figs 11a and b). Two major concentrations of maxima directions are found around the azimuth intervals 0°–10° and 70°–80°, which are different from the most recurrent directions of SSR maxima (95° and 155°). This suggests that directional maxima of ground motion are likely influenced by source location and properties. Indeed, the sources of both seismic events and noise can generate polarized waves at different frequencies, according to their mechanism and size. These polarized waves orient ground motion maxima at different frequencies in directions depending on location and mechanism of the sources that most energized spectral response at such frequencies. This phenomenon can be recognized in site responses not showing a preferential directivity, which could mask the scattering of source-controlled polarization, as shown discussing Figs 6 and 7. Therefore, in absence of an isotropic distribution of sources, no single directional curve of $\overline{\text{HVIP}_\text{R}}$ can give a complete information on site response at any frequencies.

To have some general indications, one could consider a curve derived by averaging, for each frequency, the HVIP_R values

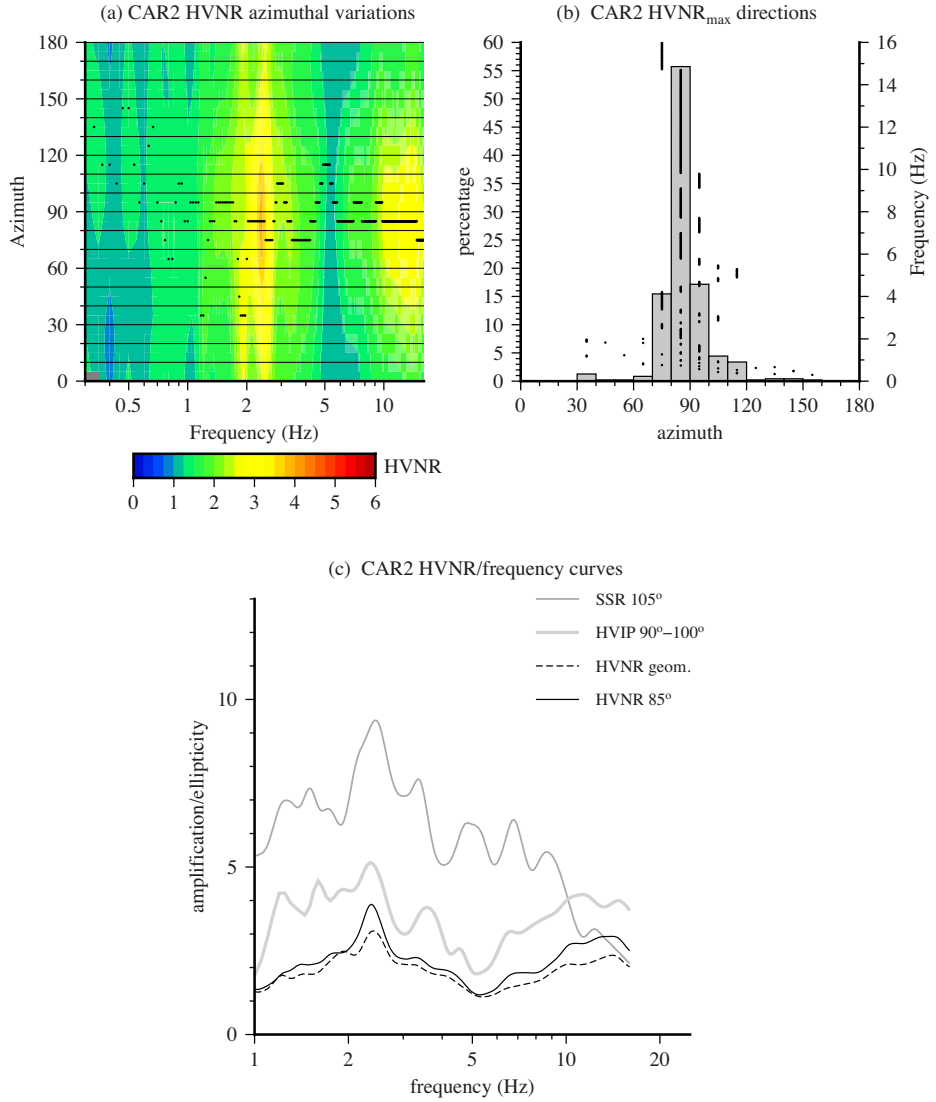

Figure 10. Results of the HVNR analysis (following the Nakamura's method) of the noise recording acquired at CAR2. Diagram (a) reports the mean values of the horizontal-to-vertical spectral ratio of noise recording ($\overline{\text{HVNR}}$) as function of frequency and azimuth. The histogram (b) shows the percentages of the frequencies having the $\overline{\text{HVNR}}$ maximum directed within different azimuth intervals. Both in (a) and (b), black dots mark the azimuth for which the maximum spectral ratio was found at each analysed frequency. Diagram (c) reports the curves of the $\overline{\text{HVNR}}$ values obtained for an azimuth of 85° (black solid line) and for the geometric mean of the horizontal components (black dashed line). For comparison purposes, the SSR curve corresponding to the maximum amplification (dark grey thin line) and the $\overline{\text{HVIP}_\text{R}}$ curve corresponding to the maximum ellipticity (light grey thick line) are also shown.

obtained in all directions. Such a curve shows a maximum at 3.4 Hz (Fig. 11c), in good agreement with the frequency of maximum amplification indicated by SSR values. However, as consequence of directional variations of $\overline{\text{HVIP}_\text{R}}$, the averaging operation tends to underestimate the ellipticity measurement and to cancel details on secondary peaks. If one examines the $\overline{\text{HVIP}_\text{R}}$ curve for the azimuth interval 170°–180° (Fig. 11c), which has a maximum close to the peak frequency of the average curve (i.e. at 3.5 Hz), the ellipticity peak value appears larger than for the average curve. Furthermore, details at least on some of the secondary peaks can be recognized, which are consistent with those resulting from SSR values.

The results of the HVIP analysis were also compared with those obtained with the Nakamura's technique, applied to the same recording. The analysis of directional variation, again, do not reveal any clear preferential directivity of HVNR maxima (Figs 12a and b), which confirms the method capability of distinguishing sites where directional resonance is present or not. However, if one examines the HVNR curve for the geometric mean of the two horizontal components, the occurrence of amplification conditions would not be recognized. Indeed, no significant peak is present at the frequency (3.3 Hz) for which the SSR data revealed a maximum amplification by a factor of about 9 (Fig. 12c). This result confirms that the standard procedure adopted by the Nakamura's method works properly if both site response and noise source distribution is isotropic.

In presence of an azimuthally irregular distribution of noise sources around the measurement station, a directional analysis of HVNR values allows recognizing the main resonance frequency. Indeed, a quite clear maximum of 3.2 is found in H/V spectral ratio at 3.6 Hz, in agreement with the frequencies resulting from SSR and HVIP analysis (3.3 and 3.5 Hz, respectively). However, this maximum is much smaller than the maximum ellipticity provided by the HVIP analysis (4.9), and no other secondary peak can be clearly distinguished.

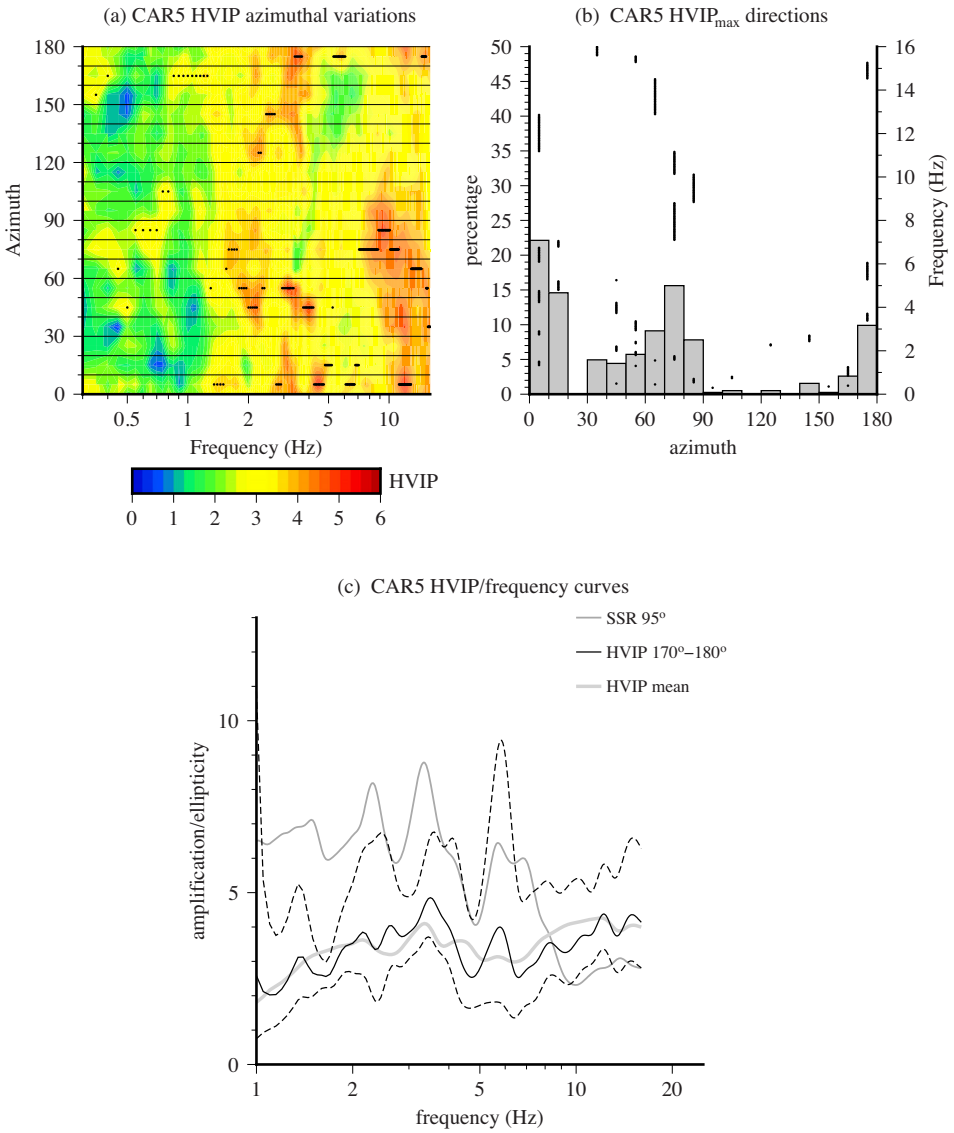

Figure 11. Results of the HVIP analysis of the noise recording acquired at CAR5. Diagram (a) reports $\overline{\text{HVIP}_R}$ values as function of frequency and azimuth. Histogram (b) shows the percentages of the frequencies having the $\overline{\text{HVIP}_R}$ maximum directed within different azimuth intervals. Both in (a) and (b), black dots mark the azimuth for which the maximum spectral ratio was found at each analysed frequency. Diagram (c) reports the curves of $\overline{\text{HVIP}_R}$ as function of frequency for the azimuth intervals 170°–180° (black solid line) and for the average calculated over all directions (light grey thick line). For the former, the black dashed lines delimit the band of variability of HVIP_R values within one standard deviation (in logarithmic residuals) from the average $\overline{\text{HVIP}_R}$. For comparison purposes, the SSR curve corresponding to maximum amplification is also shown (dark grey thin line).

3.2.3 CAR1

The site CAR1 is located on an outcrop of the formation constituting the landslide substratum, where SSR values are lower (about 7 at most) than in previous cases. This confirms the role of the colluvium layer in amplifying CAR2 and CAR5 site response. As in the case of CAR5, the results of the HVIP analysis, consistently with SSR data, do not show a preferential direction of maximum amplification (Figs 13a and b). Thus, no $\overline{\text{HVIP}_R}$ curve, calculated along any azimuthal direction, is completely representative of the site response properties.

While the SSR values show the merging of three peaks, which form a significantly amplified frequency band (SSR values larger than 4 between 5 and 9 Hz), such a complex pattern is only grossly reflected by the results of the noise analysis. Some similarities can be found between HVIP and SSR curves calculated along certain directions. For instance (Fig. 13c), for the azimuth interval 10°–20°, the $\overline{\text{HVIP}_R}$ curve shows a weak maximum close to the frequency of the SSR peak (∼7 Hz) that was found in direction 155°. Moreover, for the azimuth interval 40°–50°, the pattern of the $\overline{\text{HVIP}_R}$ curve between 5 and 9 Hz is similar to that of SSR curve in the direction (55°) of the secondary maximum at 5.7 Hz. Overall, however, it seems rather difficult to obtain from HVIP analysis a complete and reliable definition of such a complex site response, including multiple differently oriented peaks.

The analysis of the same noise recording with the Nakamura's method (Fig. 14) gives worst results. They show small peaks (H/V ∼3) only at frequencies that, according to SSR data are not significantly amplified (e.g. around 2 Hz in direction 125°: Fig. 14c) and fails completely to recognize the occurrence of significant amplification between 5 and 9 Hz (which, on the contrary, HVIP analysis was able to point out). These difficulties can derive from the lacking

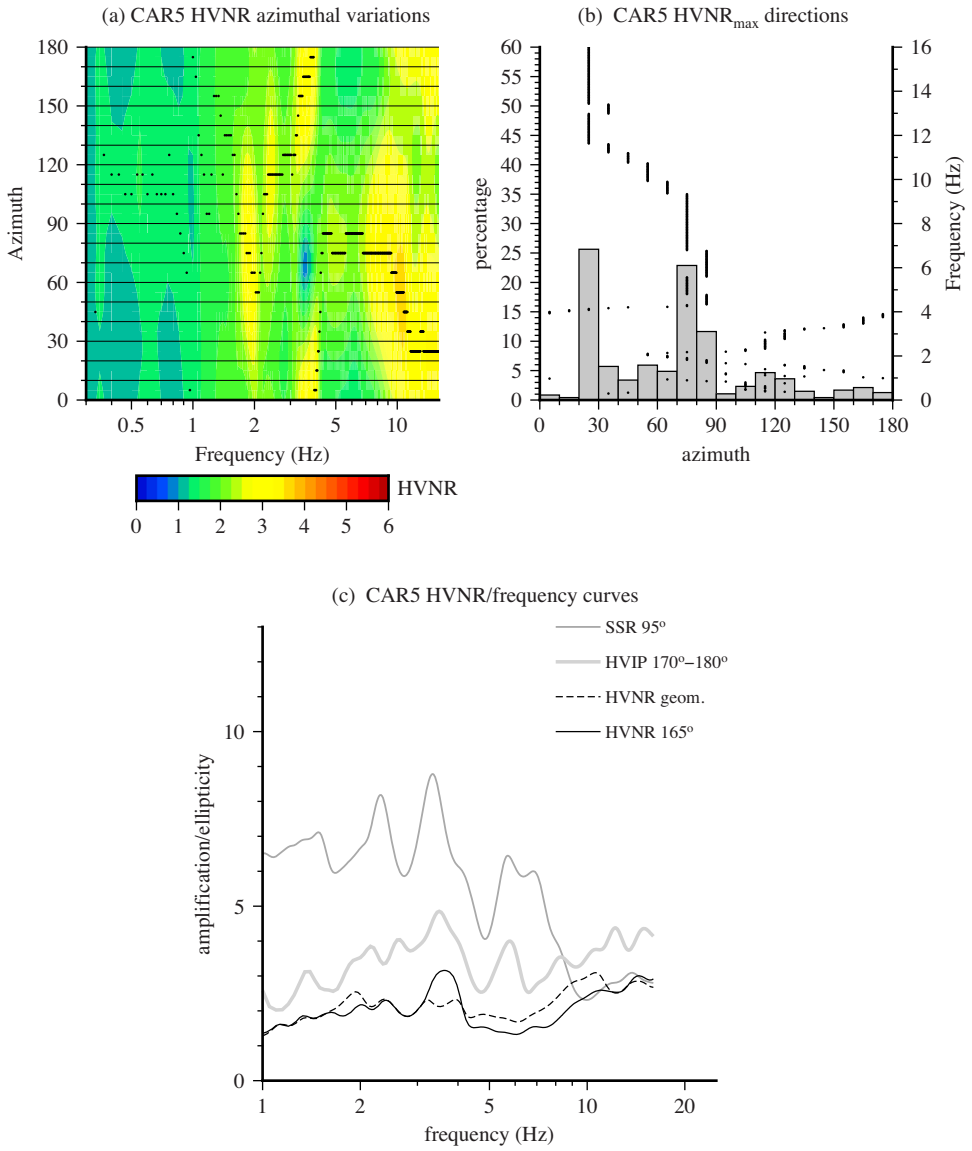

Figure 12. Results of the HVNR analysis of the noise recording acquired at CAR5. Diagram (a) reports the mean values of $\overline{\text{HVNR}}$ as function of frequency and azimuth. The histogram (b) shows the percentages of the frequencies having the $\overline{\text{HVNR}}$ maximum directed within different azimuth intervals. Both in (a) and (b), black dots mark the azimuth for which the maximum spectral ratio was found at each analysed frequency. Diagram (c) reports the curves of the $\overline{\text{HVNR}}$ values obtained for an azimuth of 165° (black solid line) and for the geometric mean of the horizontal components (black dashed line). For comparison purposes, the SSR curve corresponding to the maximum amplification (dark grey thin line) and the $\overline{\text{HVIP}_\text{R}}$ curve corresponding to the maximum ellipticity (light grey thick line) are also shown.

of noise sources sufficiently energizing the frequency band of maximum site amplification. Such unfavourable conditions appear to penalize the effectiveness of HVNR estimates more than the HVIP outcomes.

3.2.4 CAR3

The site response at CAR3 appears simpler, with a single clear peak (SSR = 13.6) at a relatively high frequency (12.6 Hz) with a sharp directional maximum along an azimuth of 125°. This is well reflected by the results of the HVIP analysis (Fig. 15), which show a pronounced maximum at a similar frequency (12.9 Hz) and direction (azimuth interval 130°–140°). The $\overline{\text{HVIP}_\text{R}}$ curve shows also an anomalous secondary peak at 2.5 Hz, but it can be disregarded as poorly constrained, considering its huge standard deviation.

In this case, even the maximum ellipticity value (12.1) is quite close to the maximum SSR value. At this regard, it is noteworthy that, for a correct definition of this maximum, it was needed to adopt a rectilinearity threshold (*rlim*) much higher (0.97) than in previous cases (see Table 2). Indeed, at the peak frequency of the CAR3 recording, a large number of HVIP_R estimates provided values larger than 10, which, setting *rlim* to 0.90, would be excluded from the calculation of the average $\overline{\text{HVIP}_\text{R}}$. In this case, the adoption of a threshold equal to 0.97 was based on the observation that the use of thresholds larger than this limit does not determine a further significant increase of the $\overline{\text{HVIP}_\text{R}}$ peak value.

The concentration of $\overline{\text{HVIP}_\text{R}}$ maxima on a preferential direction is not so marked as at CAR2 (see Fig. 15b). This might be due to the presence of amplification only in a single band of high frequencies. At lower frequencies, ellipticity has directional maxima scattered

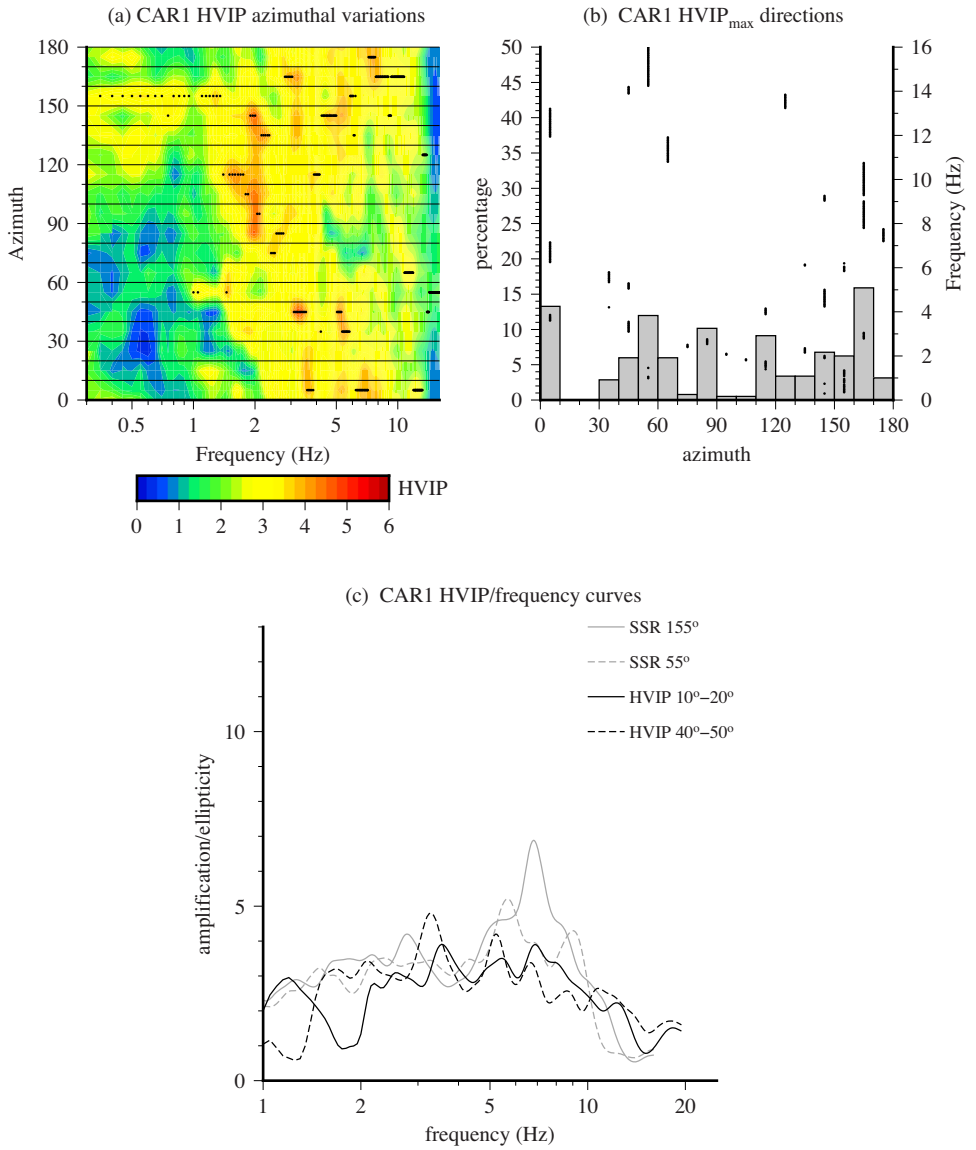

Figure 13. Results of the HVIP analysis of the noise recording acquired at CAR1. Diagram (a) reports $\overline{\text{HVIP}_\text{R}}$ values as function of frequency and azimuth. Histogram (b) shows the percentages of the frequencies having the $\overline{\text{HVIP}_\text{R}}$ maximum directed within different azimuth intervals. Both in (a) and (b), black dots mark the azimuth for which the maximum spectral ratio was found at each analysed frequency. Diagram (c) reports the curves of $\overline{\text{HVIP}_\text{R}}$ as function of frequency for the azimuth intervals 10°–20° (black solid line) and 40°–50° (black dashed line). For comparison purposes, two SSR curves are shown, which correspond to the direction of maximum amplification (155°, grey solid line) and to a secondary peak (55°, grey dashed line).

among different directions, but such maxima have very low values, which indicates the absence of significant amplification phenomena. Thus, there is a good resemblance between SSR and $\overline{\text{HVIP}_\text{R}}$ curves calculated along the maximum direction (apart from the unreliable peak at 2.5 Hz: see Fig. 15c).

For a simple site response like this, the Nakamura's technique gives good results as well, provided that a directional analysis is carried out (Fig. 16). These results provide an estimate of H/V maximum equal to the maximum ellipticity derived from the HVIP analysis at a similar frequency (12.5 Hz) and in the same direction (135°).

4 DISCUSSION

The implementation of the HVIP analysis requires the definition of some parameters: (i) the factor β controlling the filtering bandwidth; (ii) the maximum admissible deviation of planarity vector from horizontality (*ldipp*); (iii) the minimum number of consecutive samples with coherent polarization (*nmin*) and (iv) the rectilinearity threshold (*rlim*) separating Rayleigh from Love waves.

Table 2 summarizes the values of these parameters that, at each site, gave the minimum scatter of $\overline{\text{HVIP}_\text{R}}$ estimates on a set of data samples not less than 1 per cent of the total recording. In general, it appears that the optimal combination of values changes from case to case. Thus, preliminary trials are needed to evaluate which parameter combination provides a minimum scattering over a data set large enough to obtain a reliable outcome.

First tests suggest that a larger filtering bandwidth is needed when the signal/noise ratio is lower, here intending as noise the signal part that does not show a Rayleigh-type polarization. Indeed, larger β values were the optimal choices for recordings that provided a lower number of Rayleigh-type data grouped in shorter wave packets (see

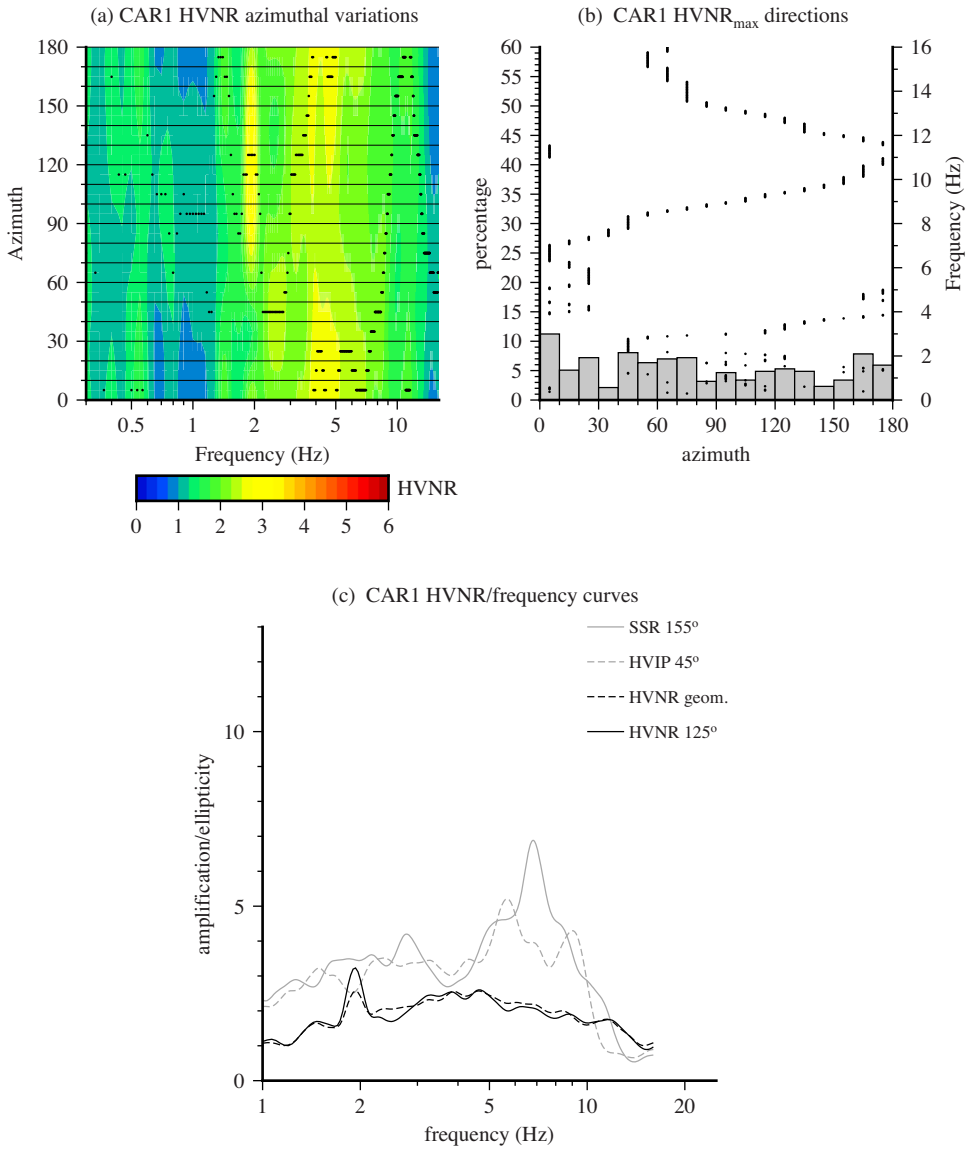

Figure 14. Results of the HVNR analysis of the noise recording acquired at CAR1. Diagram (a) reports the mean values of $\overline{\text{HVNR}}$ as function of frequency and azimuth. The histogram (b) shows the percentages of the frequencies having the $\overline{\text{HVNR}}$ maximum directed within different azimuth intervals. Both in (a) and (b), black dots mark the azimuth for which the maximum spectral ratio was found at each analysed frequency. Diagram (c) reports the curves of the $\overline{\text{HVNR}}$ values obtained for an azimuth of 125° (black solid line) and for the geometric mean of the horizontal components (black dashed line). For comparison purposes, the SSR curve corresponding to the maximum amplification (dark grey thin line) and the $\overline{\text{HVIP}}_{\text{R}}$ curve corresponding to the maximum ellipticity (light grey thick line) are also shown.

nRav and *nRp* in Table 2), likely as the effect of a higher noise level.

The choice of *nmin* seems less critical. The main purpose of using such a threshold is to remove very short time-series that could consist of incoherent noise passing the Rayleigh wave identification criteria by chance. This result can be obtained by adopting *nmin* values of the order of 10–20, which correspond to intervals of 0.1–0.2 s, significantly shorter than the mean length of wave packets identified as Rayleigh-type (see *nRp* values in Table 2). Different choices within this range does not substantially modify the results.

As shown by the case of the CAR3 site, the choice of the rectilinearity threshold *rlim* requires some more caution, since it can influence the estimate of the peak value of ellipticity. Indeed, this threshold could exclude Rayleigh waves at frequencies very close to resonance conditions, for which ellipticity tends to infinity. However, choosing a large enough *rlim* value, so that a further increase does not result in substantial variations of the ellipticity peak, the shape resulting for the $\overline{\text{HVIP}}_{\text{R}}$ curve is not significantly altered. Actually, in real data, H/V ratios can never show an infinite value, since, as effect of the presence of other noise sources, the amplitude of vertical component does not vanish. Therefore, the *rlim* value just defines the level of the 'clipping' applied to the ellipticity singularity around the resonance frequency.

Tests results showed that most of an ambient noise recording consists of signals without a coherent type of polarization (see example in Fig. 1 and data in Table 2), possibly as effect of the overlapping of different kinds of waves. A typical Rayleigh-type polarization is found only in a small fraction of the recording samples and, on average, for time intervals shorter than 1 s. These intervals likely correspond to the arrival of the most energetic part of Rayleigh

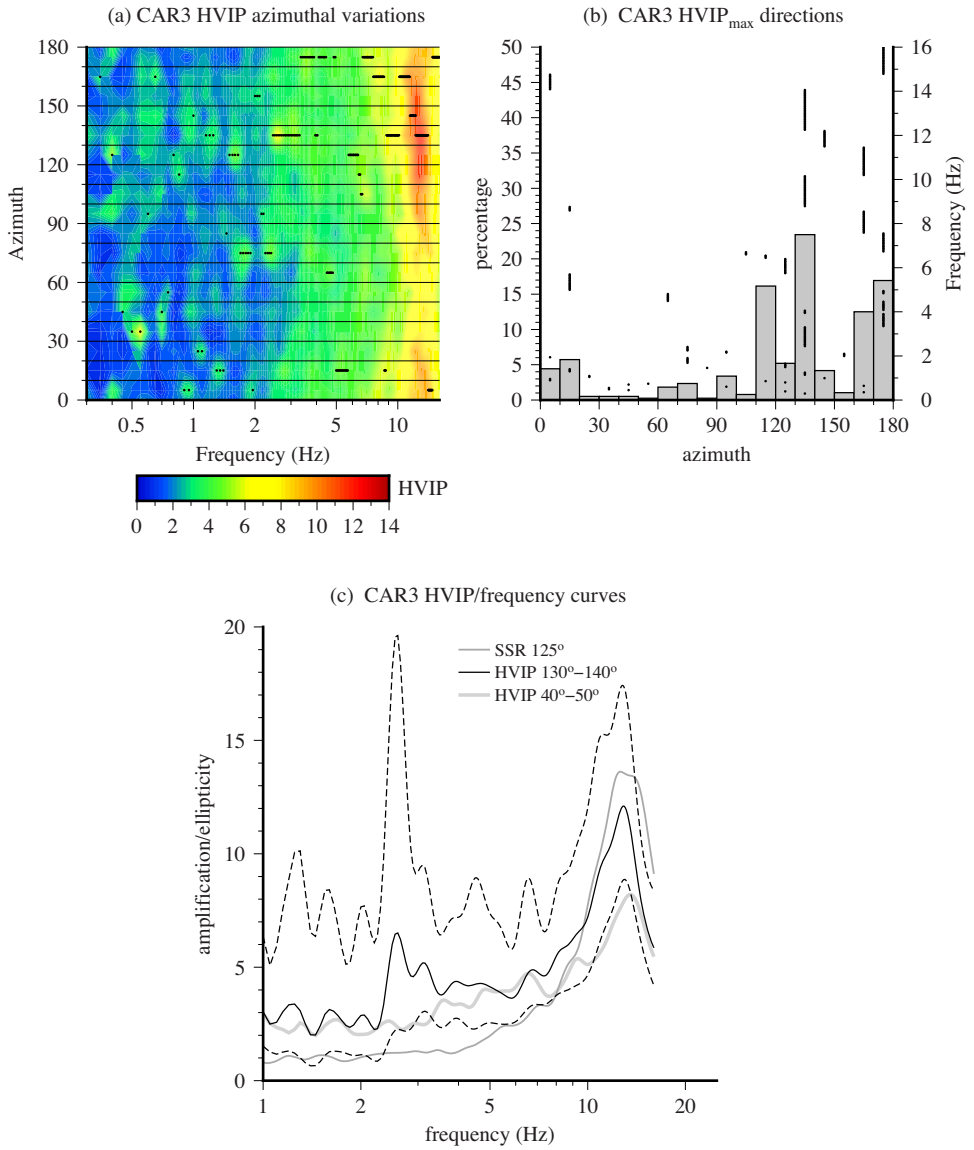

Figure 15. Results of the HVIP analysis of the noise recording acquired at CAR3. Diagram (a) reports $\overline{\text{HVIP}_R}$ values as function of frequency and azimuth. Histogram (b) shows the percentages of the frequencies having the $\overline{\text{HVIP}_R}$ maximum directed within different azimuth intervals. Both in (a) and (b), black dots mark the azimuth for which the maximum spectral ratio was found at each analysed frequency. Diagram (c) reports the curves of $\overline{\text{HVIP}_R}$ as function of frequency for the azimuth intervals 130°–140° (black solid line) and 40°–50° (light grey thick line). For the former, the black dashed lines delimit the band of variability of HVIP_R values within one standard deviation (in logarithmic residuals) from the average $\overline{\text{HVIP}_R}$. For comparison purposes, the SSR curve corresponding to maximum amplification is also shown (dark grey thin line).

wave packets, during which their polarization prevails over that of the incoherent background noise. This explains the difference of results in comparison to the Nakamura's method, which provides H/V estimates averaged over tens of seconds, corresponding to the length of the recording partitions, during which Rayleigh waves can be mixed to other types of waves.

These peculiarities of ambient noise characteristics, observed in first tests carried out on real data, motivated the adoption of the approach proposed in this study for the analysis of ambient noise in site response investigation. The HVIP method has analogies with other techniques of polarization analysis previously proposed by other authors. Some of these techniques (e.g. Jurkevics 1988) have been mainly employed in site response investigations based on the analysis of earthquake recordings (e.g. Pischiutta *et al*. 2012) or, when applied to seismic noise analysis, to estimate directions of ground motion polarization (e.g. Di Giulio *et al*. 2009; Pischiutta *et al*. 2015). Although the method in principle can be used also to calculate ellipticity of Rayleigh waves, it does not provide instantaneous estimates and, for time-domain analysis, needs to be applied to sliding time windows, so that the analysis implies an averaging over such time windows. While this can be an adequate choice for the analysis of earthquake seismograms, in the case of ambient noise the averaging, even over short time windows, can include a mix of Rayleigh waves with other types of signals. Data of Table 2 show that, taking into account the acquisition rate of 128 samples per second, the mean length of Rayleigh wave packets identified in the test sites was between 0.2 and 0.9 s.

More similar to the HVIP approach is that proposed by Vidale (1986), which also allows the estimate of instantaneous properties of the particle motion. Although originally proposed for the

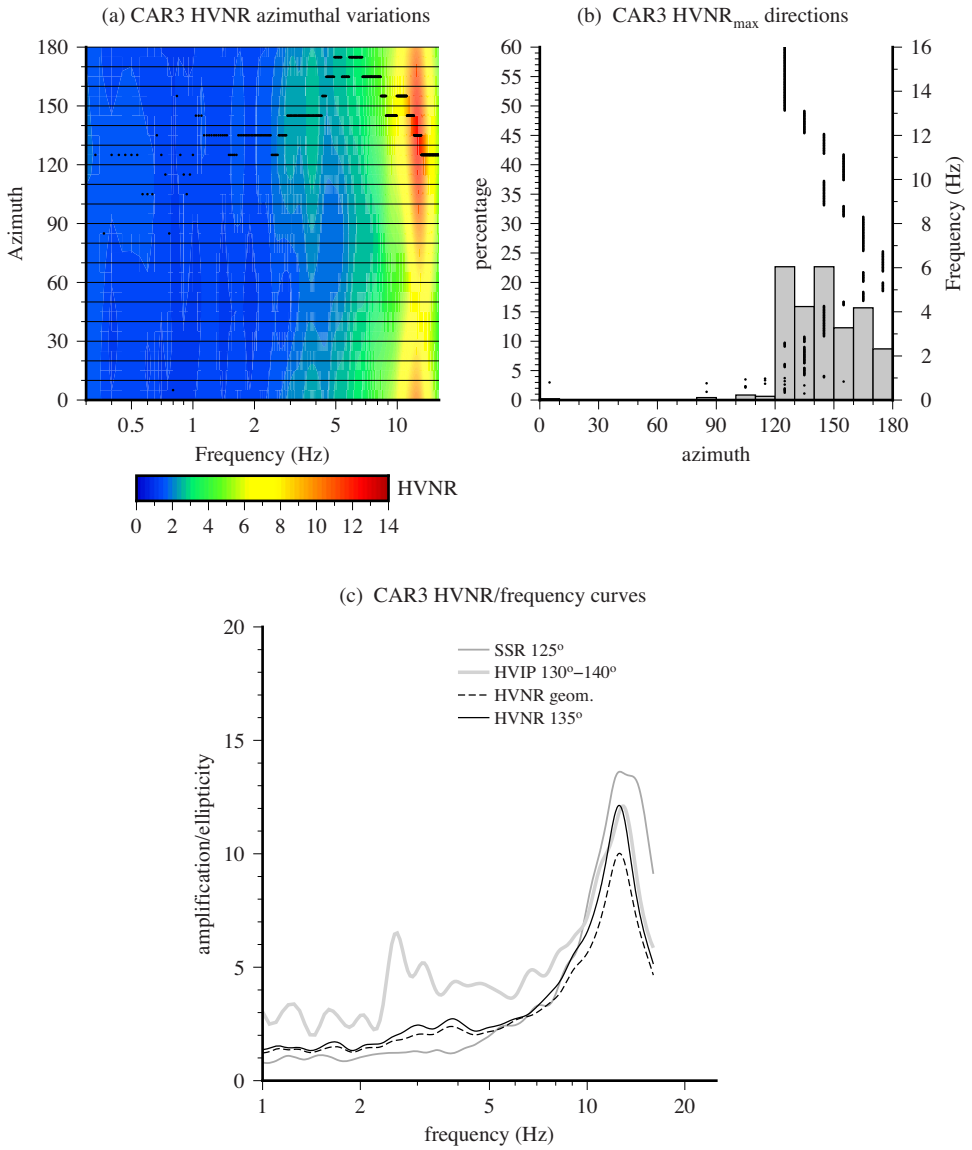

Figure 16. Results of the HVNR analysis of the noise recording acquired at CAR3. Diagram (a) reports the mean values of $\overline{\text{HVNR}}$ as function of frequency and azimuth. The histogram (b) shows the percentages of the frequencies having the $\overline{\text{HVNR}}$ maximum directed within different azimuth intervals. Both in (a) and (b), black dots mark the azimuth for which the maximum spectral ratio was found at each analysed frequency. Diagram (c) reports the curves of the $\overline{\text{HVNR}}$ values obtained for an azimuth of 135° (black solid line) and for the geometric mean of the horizontal components (black dashed line). For comparison purposes, the SSR curve corresponding to the maximum amplification (dark grey thin line) and the $\overline{\text{HVIP}}_{\text{R}}$ curve corresponding to the maximum ellipticity (light grey thick line) are also shown.

analysis of earthquake recordings, it was also applied to ambient noise (e.g. Burjanek *et al*. 2010). The HVIP approach differs from this technique because polarization analysis is applied simultaneously to the three components of the recording only for the identification of Rayleigh wave packets. Instead, to estimate their ellipticity, analytic transformation is separately applied to the horizontal components (to calculate H_{max}) and to the vertical one (to calculate the amplitude V). In this way, one can reduce the errors in ellipticity estimates induced by incoherent background noise contaminating Rayleigh waves. These contaminations determine: (i) the deviations of the plane of the Rayleigh wave particle motion from verticality, (ii) the deviations of the axes of the elliptical trajectory from horizontal/vertical directions and (iii) the deviations of the horizontal component of Rayleigh waves from rectilinearity. The effect of this disturbing noise should be reduced if the ratio H_{max}/V is calculated instead of the ratio a/b between the axes of the elliptical trajectory. This improvement can be properly expected if the recording station is located on a subhorizontal surface. However, in case of strongly inclined surfaces, adaptations can be easily taken into account, once the surface inclination is measured.

The results of first tests on sites with known site response properties have indicated that the HVIP technique has a good capacity of revealing the occurrence of site response directivity, providing correct identification of frequency and orientation of directional resonance. For one site (CAR2), it was possible to check the plausibility of the estimates of the Rayleigh wave ellipticity, finding values compatible with velocity models obtained from independent data.

Some caution is however needed in interpreting data acquired in a single recording. Indeed, one cannot exclude that results may be biased by the presence of sources exciting strongly polarized signals

in a wide frequency range (e.g. as the results of dominant winds causing oscillations of differently high objects, like trees, poles or buildings, in the same direction with different oscillation periods). Therefore, as general recommendation, the HVIP analysis should be conducted on more recordings acquired under different environmental conditions, possibly on more sites simultaneously, to assess whether the $\overline{\mathrm{HVIP}_\mathrm{R}}$ curves really reflect persistent site-specific properties of ground vibration, rather than polarization properties controlled by noise source characteristics.

More uncertainties affect the definition of the ellipticity curve at sites where the dynamic response show multiple and differently oriented maxima. This can be due to the presence of more factors controlling amplification at different frequencies, which either have a different directionality or, even acting isotropically, are revealed only along directions of source-controlled wave polarizations. In such cases, a correct interpretation of HVIP analysis can be difficult, especially if noise sources do not energize the entire spectral band analysed and if they have an anisotropic spatial distribution around the recording station. Indeed, in such cases, neither the $\overline{\mathrm{HVIP}_\mathrm{R}}$ curves obtained along any selected azimuth, nor a curve averaging Rayleigh-type signals with any polarization are representative of the real ellipticity curve for the entire frequency band examined. Thus, the main limitations to the employment of the HVIP technique appear related to the possible occurrence of unfavourable conditions of noise excitation during data acquisition, which can make more uncertain the reliability of data interpretation.

It should be underlined that this analysis technique was mainly devised to draw information on complex site response, differing from resonance at sites with flat horizontal layering, which are typically investigated with the Nakamura's technique. First tests conducted on sites with complex site response showed that the HVIP methods seems to perform better in revealing site response characterized by multiple resonance frequencies with site-specific directivity, in comparison to the Nakamura technique. Indeed, the latter seems to provide a less detailed information on spectral response (as in the case of the sites CAR2 and CAR5) or may even fail to recognize resonance conditions (as in the case of the site CAR1) that the HVIP analysis was able to point out. Instead, the performance of the two techniques appear comparable in case of site response characterized by a single sharp maximum (as in the case of the site CAR3).

5 CONCLUSIONS

This study proposes a procedure for ambient noise analyses aimed at investigating complex cases of site response, characterized my multiple resonance frequencies with directional variations of amplification. The proposed procedure is based on the analysis of instantaneous polarization of ambient noise recordings, applied after having passed such recordings through narrow-band filters, centred on different central frequencies. Polarization properties are used first to identify wave packets of Rayleigh waves and then to determine their ellipticity and polarization direction as function of frequency. In particular, ellipticity is calculated as the ratio between the maximum amplitude of ground motion on the horizontal plane and the amplitude of the vertical component, both derived from the analytic transformation of the recording components. For the identification of Rayleigh waves, this method requires the definition of some threshold parameters, which are selected through preliminary trials aimed at obtaining a large data set with a minimum scattering of ellipticity values.

First test results indicate that only a small percentage of noise recordings, dispersed through several intervals of some tenths of seconds, shows a Rayleigh-type particle motion, possibly when the energy carried by these waves prevails on the incoherent background noise. This justifies the adoption of an approach based on instantaneous estimates as more effective than techniques that average noise characteristics over time windows of the order of seconds.

From the variation of the mean ellipticity values $\overline{\mathrm{HVIP}_\mathrm{R}}$ with azimuth and frequency, obtained from a large number of data (in the order of thousands), information can be inferred on directional variations of site response characteristics. In particular, the presence of a preferential orientation of Rayleigh wave direction, combined with pronounced peaks of $\overline{\mathrm{HVIP}_\mathrm{R}}$ at certain frequencies, can reveal the occurrence of directional resonance conditions. The amplitude of the $\overline{\mathrm{HVIP}_\mathrm{R}}$ peaks does not represent a direct measurement of the amplification factor, even though is correlated to it so that the occurrence of larger amplification can be inferred from larger ellipticity values. Additionally, the ellipticity curve can provide constraints to determine vertical distribution of body wave velocity, which offers indirect information on the amplification factors.

The results of tests carried out on sites with known response properties showed that the HVIP method has a good capacity of revealing frequency and orientation of directional resonance. The definition of the ellipticity curve at sites whose dynamic response is characterized by multiple directional maxima with different orientation appears more problematic. In such cases, depending on the azimuthal distribution of sources exciting noise at different frequencies, some information on site response can be missed, even though, in comparison to the Nakamura's method, this new technique seems able to provide some more details on spectral properties of sites.

At this stage, the HVIP method is proposed as a new method of processing ambient noise data in site response investigations. Furthermore, the results of this kind of analysis offer additional elements to check hypotheses on ambient noise origin, providing constraints to its modelling. Further experiments on real data in a variety of site conditions will be needed to confirm its validity and to explore potential and limits of its applicability: this will be object of future studies.

ACKNOWLEDGEMENTS

Constructive comments of the editor Martin Schimmel, Marta Pischiutta and an anonymous referee stimulated a considerable improvement of this manuscript.

REFERENCES

Albarello, D. & Lunedei, E., 2009. Alternative interpretations of horizontal to vertical spectral ratios of ambient vibrations: new insights from theoretical modeling, *Bull. Earthq. Eng.,* **8,** 519–534.

Bard, P.-Y., 1999. Microtremor measurements: a tool for site effect estimation?, in *The Effects of Surface Geology on Seismic Motion,* pp. 1251–1279, eds Irikura, K., Kudo, K., Okada, H. & Sasatani, T., Balkema, Rotterdam.

Bard, P.Y. & the SESAME Team, 2004. Guidelines for the implementation of the H/V spectral ratio technique on ambient vibrations: measurements, processing and interpretation, *SESAME European Research Project, WP12—Deliverable D23.12*. Available at: ftp://ftp.geo.uib.no/pub/seismo/SOFTWARE/SESAME/USER-GUIDELINES/SESAME-HV-User-Guidelines.pdf, last access 24 May, 2017.

Bonamassa, O. & Vidale, J.E., 1991. Directional site resonances observed from aftershocks of the 18 October 1989 Loma Prieta earthquake, *Bull. seism. Soc. Am.,* **81**(5), 1945–1957.

Bonnefoy-Claudet, S., Cotton, F. & Bard, P.-Y., 2006a. The nature of seismic noise wavefield and its implications for site effects studies—a literature review, *Earth-Sci. Rev.,* **79,** 205–227.

Bonnefoy-Claudet, S., Cornou, C., Bard, P.-Y., Cotton, F., Moczo, P., Kristek, J. & Fäh, D., 2006b. H/V ratio: a tool for site effects evaluation. Results from 1-D noise simulations, *Geophys. J. Int.,* **167,** 827–837.

Bonnefoy-Claudet, S., Köhler, A., Cornou, C., Wathelet, M. & Bard, P.-Y., 2008. Effects of Love waves on microtremor H/V ratio, *Bull. seism. Soc. Am.,* **98,** 288–300.

Borcherdt, R.D., 1970. Effects of local geology on ground motion near San Francisco Bay, *Bull. seism. Soc. Am.,* **60**(1), 29–61.

Buccolini, M., Fiorillo, F., Lollino, G., Rusi, S., Sciarra, N. & Wasowski, J., 1995. *La frana di Caramanico Terme dell'ottobre 1989*, Dipartimento di Scienze, Università "G. d'Annunzio", Pescara.

Burjánek, J., Gassner-Stamm, G., Poggi, V., Moore, J.R. & Fäh, D., 2010. Ambient vibration analysis of an unstable mountain slope, *Geophys. J. Int.,* **180,** 820–828.

Castellaro, S. & Mulargia, F., 2009. VS_{30} estimates using constrained H/V measurements, *Bull. seism. Soc. Am.,* **99**(2A), 761–773.

Coccia, S., Del Gaudio, V., Venisti, N. & Wasowski, J., 2010. Application of Refraction Microtremor (ReMi) technique for determination of 1-D shear wave velocity in a landslide area, *J. appl. Geophys.,* **71,** 71–89.

Cultrera, G., Rovelli, A., Mele, G., Azzara, R., Caserta, A. & Marra, F., 2003. Azimuth-dependent amplification of weak and strong ground motion within a fault zone (Nocera Umbra, central Italy), *J. geophys. Res.,* **108**(B3), 2156–2170.

Del Gaudio, V. & Wasowski, J., 2007. Directivity of slope dynamic response to seismic shaking, *Geophys. Res. Lett.,* **34,** L12301, doi:10.1029/GL029842.

Del Gaudio, V. & Wasowski, J., 2011. Advances and problems in understanding the seismic response of potentially unstable slopes, *Eng. Geol.,* **122,** 73–83.

Del Gaudio, V., Coccia, S., Wasowski, J., Gallipoli, M.R. & Mucciarelli, M., 2008. Detection of directivity in seismic site response from microtremor spectral analysis, *Nat. Hazards Earth Syst. Sci.,* **8,** 751–762.

Del Gaudio, V., Wasowski, J. & Muscillo, S., 2013. New developments in ambient noise analysis to characterise the seismic response of landslide prone slopes, *Nat. Hazards Earth Syst. Sci.,* **13,** 2075–2087.

Del Gaudio, V., Muscillo, S. & Wasowski, J., 2014. What we can learn about slope response to earthquakes from ambient noise analysis: an overview, *Eng. Geol.,* **182,** 182–200.

Di Giulio, G., Cara, F., Rovelli, A., Lombardo, G. & Rigano, R., 2009. Evidences for strong directional resonances in intensely deformed zones of the Pernicana fault, Mount Etna, Italy, *J. geophys. Res.,* **114,** B10308, doi:10.1029/2009JB006393.

Fäh, D., Kind, F. & Giardini, D., 2001. A theoretical investigation of average H/V ratios, *Geophys. J. Int.,* **145,** 535–549.

Jurkevics, A., 1988. Polarization analysis of three-component array data, *Bull. seism. Soc. Am.,* **78**(5), 1725–1743.

Konno, K. & Ohmachi, T., 1998. Ground motion characteristics estimated from spectral ratio between horizontal and vertical components of microtremor, *Bull. seism. Soc. Am.,* **88**(1), 228–241.

Kramer, S., 1996. *Geotechnical Earthquake Engineering*, Prentice Hall, Upper Saddle River, New Jersey.

Louie, J.N., 2001. Fater, Better: Shear wave velocity to 100 meters depth from refraction microtremor arrays. *Bull. seism. Soc. Am.,* **91**(2), 347–364.

Martino, S., Minutolo, A., Paciello, A., Rovelli, A., Scarascia Mugnozza, G. & Verrubbi, V., 2006. Evidence of amplification effects in fault zone related to rock mass jointing, *Nat. Hazards,* **39,** 419–449.

Moore, J.R., Gischig, V., Burjanek, J., Loew, S. & Fäh, D.; 2011. Site effects in unstable rock slopes: dynamic behavior of the Randa instability (Switzerland), *Bull. seism. Soc. Am.,* **101**(6), 3110–3116.

Morozov, I.B. & Smithson, S.B.1996. Instantaneous polarization attributes and directional filtering, *Geophysics,* **61,** 872–881.

Nakamura, Y., 1989. A method for dynamic characteristics estimation of subsurface using microtremor on the ground surface, *Q. Rep. Railw. Tech. Res. Inst.,* **30,** 25–33.

Nogoshi, M. & Igarashi, T., 1971. On the amplitude characteristics of microtremor (part 2) (in Japanese with English abstract), *J. Seismol. Soc. Japan,* **24,** 26–40.

Panzera, F., D'Amico, S., Lotteri, A., Galea, P., Lombardo & G., 2012. Seismic site response of unstable steep slope using noise measurements: the case study of Xemxija bay area, Malta, *Nat. Hazards Earth Syst. Sci*., **12,** 3421–3431.

Pischiutta, M., Salvini, F., Fletcher, J., Rovelli, A. & Ben-Zion, Y., 2012. Horizontal polarization of ground motion in the Hayward fault zone at Fremont, California: dominant fault-high-angle polarization and fault-induced cracks, *Geophys. J. Int.,* **188**(3), 1255–1272.

Pischiutta, M., Savage, M.K., Holt, R.A. & Salvini, F., 2015. Fracture-related wavefield polarization and seismic anisotropy across the Greendale Fault, *J. geophys. Res.,* **120,** 7048–7067.

Poggi, V., Fäh, D., Burjánek, J. & Giardini, D., 2012. The use of Rayleigh-wave ellipticity for site-specific hazard assessment and microzonation: application to the city of Lucerne, Switzerland, *Geophys. J. Int.,* **188,** 1154–1172.

Schimmel, M. & Gallart, J., 2003. The use of instantaneous polarization attributes for seismic signal detection and image enhancement, *Geophys. J. Int.,* **155,** 653–668.

Schimmel, M. & Gallart, J., 2004. Degree of polarization filter for frequency-dependent signal enhancement through noise suppression, *Bull. seism. Soc. Am.,* **94,** 1016–1035.

Schimmel, M., Stutzman, E., Ardhuin, F. & Gallart, J., 2011. Polarized Earth's ambient microseismic noise, *Geochem. Geophys. Geosyst.,* **12,** Q07014, doi:10.1029/2011GC003661.

Spudich, P., Hellweg, M. & Lee, W.H.K., 1996. Directional topographic site response at Tarzana observed in aftershocks of the 1994 Northridge, California, earthquake: implications for mainshock motions, *Bull. seism. Soc. Am.,* **86**(1B), S193–S208.

Vidale, J.E., 1986. Complex polarization analysis of particle motion, *Bull. seism. Soc. Am.,* **76**(5), 1393–1405.

Vidale, J.E., Bonamassa, O. & Houston, H., 1991. Directional site resonances observed from the 1 October 1987 Whittier Narrows, California, earthquake and the 4 October aftershock, *Earthq. Spectra,* **7,** 107–125.

Wathelet, M., 2005. Array recordings of ambient vibrations: surface-wave inversion, *PhD thesis*, Liège University, Belgium.